National Library of Canada
Bibliothèque nationale du Canada

Canadian Theses Service
Services des thèses canadiennes

Ottawa, Canada
K1A 0N4

CANADIAN THESES
THÈSES CANADIENNES

NOTICE

The quality of this microfiche is heavily dependent upon the quality of the original thesis submitted for microfilming. Every effort has been made to ensure the highest quality of reproduction possible.

If pages are missing, contact the university which granted the degree.

Some pages may have indistinct print especially if the original pages were typed with a poor typewriter ribbon or if the university sent us an inferior photocopy.

Previously copyrighted materials (journal articles, published tests, etc.) are not filmed.

Reproduction in full or in part of this film is governed by the Canadian Copyright Act, R.S.C. 1970, c. C-30. Please read the authorization forms which accompany this thesis.

AVIS

La qualité de cette microfiche dépend grandement de la qualité de la thèse soumise au microfilmage. Nous avons tout fait pour assurer une qualité supérieure de reproduction.

S'il manque des pages, veuillez communiquer avec l'université qui a conféré le grade.

La qualité d'impression de certaines pages peut laisser à désirer, surtout si les pages originales ont été dactylographiées à l'aide d'un ruban usé ou si l'université nous a fait parvenir une photocopie de qualité inférieure.

Les documents qui font déjà l'objet d'un droit d'auteur (articles de revue, examens publiés, etc.) ne sont pas microfilmés.

La reproduction, même partielle, de ce microfilm est soumise à la Loi canadienne sur le droit d'auteur, SRC 1970, c. C-30. Veuillez prendre connaissance des formules d'autorisation qui accompagnent cette thèse.

THIS DISSERTATION
HAS BEEN MICROFILMED
EXACTLY AS RECEIVED

LA THÈSE A ÉTÉ
MICROFILMÉE TELLE QUE
NOUS L'AVONS REÇUE

NL 339 (r. 86/01)

Canada

277

0-315-27008-X

National Library of Canada
Canadian Theses Division
Ottawa, Canada
K1A 0N4

Bibliothèque nationale du Canada
Division des thèses canadiennes

PERMISSION TO MICROFILM — AUTORISATION DE MICROFILMER

• Please print or type — Écrire en lettres moulées ou dactylographier

Full Name of Author — Nom complet de l'auteur

FAN CHEN YU BUSTOMI

Date of Birth — Date de naissance	Country of Birth — Lieu de naissance
FEB 1, 1959	INDONESIA

Permanent Address — Résidence fixe

JALAN KINOL NO 7
PALEMBANG INDONESIA

Title of Thesis — Titre de la thèse

EXPERIMENTAL MODELLING OF JET CUTTING OF OIL SANDS

University — Université

UNIV OF ALBERTA

Degree for which thesis was presented — Grade pour lequel cette thèse fut présentée

MSc

Year this degree conferred — Année d'obtention de ce grade	Name of Supervisor — Nom du directeur de thèse
1983	DR. GATES

Permission is hereby granted to the NATIONAL LIBRARY OF CANADA to microfilm this thesis and to lend or sell copies of the film.

The author reserves other publication rights, and neither the thesis nor extensive extracts from it may be printed or otherwise reproduced without the author's written permission.

L'autorisation est, par la présente, accordée à la BIBLIOTHÈQUE NATIONALE DU CANADA de microfilmer cette thèse et de prêter ou de vendre des exemplaires du film.

L'auteur se réserve les autres droits de publication; ni la thèse ni de longs extraits de celle-ci ne doivent être imprimés ou autrement reproduits sans l'autorisation écrite de l'auteur.

Date	Signature
OCT. 14 '83	

NL-91 (4/77)

THE UNIVERSITY OF ALBERTA

Experimental Modelling of Jet Cutting of Oil Sands

by

Chen Yu B. Fan

(C)

A THESIS

SUBMITTED TO THE FACULTY OF GRADUATE STUDIES AND RESEARCH

IN PARTIAL FULFILMENT OF THE REQUIREMENTS FOR THE DEGREE

OF Master of Science

Department of Mechanical Engineering

EDMONTON, ALBERTA

Fall 1983.

THE UNIVERSITY OF ALBERTA

RELEASE FORM

NAME OF AUTHOR Chen Yu B. Fan

TITLE OF THESIS Experimental Modelling of Jet Cutting of Oil Sands

DEGREE FOR WHICH THESIS WAS PRESENTED Master of Science

YEAR THIS DEGREE GRANTED Fall 1983

Permission is hereby granted to THE UNIVERSITY OF ALBERTA LIBRARY to reproduce single copies of this thesis and to lend or sell such copies for private, scholarly or scientific research purposes only.

The author reserves other publication rights, and neither the thesis nor extensive extracts from it may be printed or otherwise reproduced without the author's written permission.

(SIGNED) Chen yu Fan

PERMANENT ADDRESS:

JALAN KINOL NO 7

PALEMBANG

INDONESIA

DATED OCTOBER 6 1983

THE UNIVERSITY OF ALBERTA

FACULTY OF GRADUATE STUDIES AND RESEARCH

The undersigned certify that they have read, and recommend to the Faculty of Graduate Studies and Research, for acceptance, a thesis entitled Experimental Modelling of Jet Cutting of Oil Sands submitted by Chen Yu B. Fan in partial fulfilment of the requirements for the degree of Master of Science.

.....C.M. Yates.....

Supervisor

.....Roger W. Toogood.....

.....B. Sunn.....

.....M. Gyarmati.....

Date.....OCTOBER 6, 1983.....

DEDICATED TO MY PARENTS

Abstract

The objective of the present study was to obtain an empirical correlation to relate the ultimate depth to which a high pressure water jet can drill or pierce a hole into an oil sands formation to the jet parameters. To this end a laboratory apparatus was constructed to study the characteristics of confined, continuous, high pressure water jets in a down-hole type geometry. Jet dynamic pressures up to 35 MPa and nozzle sizes of 3.2, 2.4, and 1.6 mm in diameter were used. Horizontal tubes of 102, 76, 51 and 38 mm diameter and a porosity of 5% for the 51 mm tube diameter were used in the tests to simulate the hole cut by the jet. Standoff distances ranged from 0.3 to 1.7 meters.

Flow visualization observations and records of the pressure signal at the bottom of tube revealed that the water jet produced discrete impacts. From this observation it was concluded that it is most appropriate to model the jet drilling as a stochastic process and to analyze the pressure signal statistically. A correlation to predict the ultimate depth of penetration was developed based on the probability of the pressure at the cutting face exceeding a critical value for non-negligible cutting rates to occur. A linear relationship between the cutting rate and the above probability was assumed and a second correlation predicting the depth of penetration with time was developed.

The predicted depth of penetration agreed closely with the field test data for jetting times up to 60 seconds. No data is available for jetting times beyond 60 seconds. The model predicts a lower value than the correlation derived from experimental work using recompacted oil sands (Chau, 1980).

The model could not be effectively evaluated due to the limited field test results. Modelling of the jet cutting as a stochastic process appears to be an appropriate approach and is considered to give more valuable information than any cutting models based on the average or peak pressure.

ACKNOWLEDGEMENTS

The author wishes to express his sincere appreciation for the invaluable advice, guidance and supervision rendered by Dr. E.M. Gates and Dr. R.W. Toogood in the preparation of this thesis.

A special thanks to Mr. G. Rovang and Mr. M. Hilash for their assistance in constructing the test model.

Thanks are also due to Mr. A. Muir and his colleagues for their excellent work in the fabrication of the model. The author would also like to thank Mr. T. Nord for his advices and assistance in electronics devices over the entire course of development of this project.

Funding of this project was made possible by the Alberta Oil Sands Technology and Research Authority (AOSTRA).

Finally, the author is grateful to Dr. and Mrs. T.S. Fan for the overall support and encouragement throughout his study at the University of Alberta.

NOMENCLATURE

d_o	nozzle diameter
D	tube diameter
P_d	jet dynamic pressure at the nozzle
t	jetting time
tult	time to reach ultimate depth
V	average velocity of jet at the nozzle
Z	depth of penetration
Zult	ultimate depth of penetration
ρ	density of water
Q	volume flow rate
p	pressure at the cutting face
Pc	critical pressure at oil sands surface below which no further penetration occurs
B	initial cutting rate
θ	probability that the pressure p exceeds Pc
a,k	experimental constants
dZ/dt	cutting rate

Table of Contents

Chapter		Page
1.	Introduction	1
	1.1 Background Information.	1
	1.2 Present Investigation	5
2.	Experimental Apparatus and Procedures	7
	2.1 Apparatus	7
	2.2 Nozzle Assembly	13
	2.3 Nozzle Geometry	13
	2.4 Instrumentation	13
	2.4.1 Load Cell	13
	2.4.2 Signal Analysis	16
	2.5 Test Procedure	23
3.	Presentation of Results	25
	3.1 Flow Visualization	26
	3.2 Quantitative Results	32
	3.2.1 Frequency distribution	32
	3.2.2 Average pressure	40
4.	Analysis of Results	47
	4.1 Prediction of Maximum Depth of Penetration	48
	4.2 Prediction of Cutting Time	58
5.	Discussion of Results	62
	5.1 Comparisons of prediction and other correlations	62
	5.2 Influence of some assumptions in the empirical model	67
	5.3 Differences between the simulated and actual down-hole geometry	70
	5.4 Consequences of the predictions	70

5.5 Alternative model in jet cutting 73
6. Conclusions and Recommendations 78
BIBLIOGRAPHY 80
APPENDIX A 83
APPENDIX B 86

List of Tables

Table Page

5.1 Variation of the parameter between the first and second models.....77

List of Figures

Figure		Page
1.1	Comparison of predictions of the ultimate depth of penetration for an unconfined jet (after Gilpin & Gates, 1982)	6
2.1	A schematic drawing of a proposed down-hole jet piercing operation	8
2.2	A schematic diagram of the laboratory model of a down-hole jet piercing geometry	9
2.3	A schematic diagram of the nozzle geometry	15
2.4	A schematic diagram showing the load cell geometry and the positioning of the strain gauges	18
2.5	A block diagram summarizing the stages in the analysis of the load cell signal	20
3.1	A sketch illustrating the flow within the tube when no interference occurs between the incoming jet and the returning water	31
3.2	A sketch illustrating the flow within the tube when interference between the incoming jet and the spent water begins to occur	31
3.3	A sketch illustrating the flow within the tube when the presence of the slug has become continuous	31
3.4	A sketch illustrating the flow within the tube of a porous wall	31
3.5	The probability and cumulative density function of the load cell signal for increasing values of the standoff distance (D=102 mm, P_d =2.3 MPa)	33
3.6	The probability and cumulative density function of the load cell signal for increasing values of the standoff distance (D=102 mm, P_d =20.5MPa)	34
3.7	The probability and cumulative density function of the load cell signal for increasing values of the standoff distance (D=76 mm, P_d =1.8 MPa)	35

Figure Page

3.8 The probability and cumulative density function of the load cell signal for increasing values of the standoff distance (D=51 mm solid, P_d =2.2 MPa).....36

3.9 The probability and cumulative density function of the load cell signal for increasing values of the standoff distance (D=38 mm, P_d =2.1 MPa).....37

3.10 The probability and cumulative density function of the load cell signal for increasing values of the standoff distance (D=38 mm, P_d =15.6 MPa).....38

3.11 The probability and cumulative density function of the load cell for increasing values of the standoff distance (D=51 mm porous, P_d =21.4 MPa).....39

3.12 A plot of the non-dimensionalized average pressure against the non-dimensionalized standoff distance for 102 mm diameter solid wall tube.....41

3.13 A plot of the non-dimensionalized average pressure against the non-dimensionalized standoff distance for 76 mm diameter solid wall tube.....42

3.14 A plot of the non-dimensionalized average pressure against the non-dimensionalized standoff distance for 51 mm diameter solid wall tube.....43

3.15 A plot of the non-dimensionalized average pressure against the non-dimensionalized standoff distance for 51 mm diameter porous wall tube.....44

3.16 A plot of the non-dimensionalized average pressure against the non-dimensionalized standoff distance for 38 mm diameter solid wall tube.....45

4.1 Probability and cumulative density functions using the same nozzle as Chau (1980).....49

Figure Page

4.2 The probability that the pressure at the piston face exceeds the critical value for some combinations of nozzle diameter and pressure in the 102 mm diameter tube.....51

4.3 The probability that the pressure at the piston face exceeds the critical value for some combinations of nozzle diameter and pressure in the 76 mm diameter tube.....52

4.4 The probability that the pressure at the piston face exceeds the critical value for some combinations of nozzle diameter and pressure in the 51 mm diameter solid tube.....53

4.5 The probability that the pressure at the piston face exceeds the critical value for some combinations of nozzle diameter and pressure in the 51 mm diameter porous tube.....54

4.6 The probability that the pressure at the piston face exceeds the critical value for some combinations of nozzle diameter and pressure in the 38 mm diameter tube.....55

4.7 The variation of the parameter with dynamic pressure for different tube and nozzle diameters.....56

4.8 Estimates of the parameter B based upon best fits of equation (9) to the laboratory data of Chau (1980).....61

5.1 A comparison between depths of penetration predicted by equation (9) and the field data of Chau (1980) for a 6.4 mm diameter nozzle....63

5.2 An estimate of the time required to reach the predicted ultimate depth of penetration.....64

5.3 A comparison of ultimate depths predicted by the present correlation with that predicted by Gates et al. (1982).....66

5.4 The dependence of critical pressure on the critical probability chosen.....68

5.5 An estimate of the water requirements to reach the ultimate depth of penetration for various dynamic pressures.....72

Figure Page

5.6 The probability that the pressure at the piston face exceeds the critical value for alternative model.....74

5.7 The variation of the parameter with dynamic pressures between the first and second model.....75

List of Plates

Plate		Page
2.1	A photograph of the experimental apparatus used to model a down-hole jet piercing geometry. In this photograph a 38 mm diameter horizontal tube is in place and the piston to nozzle distance is 0.9 meter	10
2.2	A photograph of the apparatus arranged for porous wall tube tests. The square horizontal box enclosing the porous tube collects the water escaping through the pores	12
2.3	A photograph of the nozzle support and alignment assembly	14
2.4	A photograph of the four pistons used in these experiments	17
2.5	A photograph of the apparatus used to calibrate the load cell	19
2.6	An example oscilloscope trace of the load cell signal	22
3.1	A sequence of high speed camera frames showing the flow of an unconfined continuous jet	27

1. Introduction

1.1 Background Information.

Oil sands, also known as tar sands and bituminuous sands, have been found throughout the world, but the largest deposit, estimated at 900 billion barrels of crude bitumen, lies in the northeastern part of the Province of Alberta, Canada (Baughman, 1978). Despite the fact that this reserve has been known for many years, it is only recently that tar sands have assumed commercial importance. Difficulties encountered in mapping, exploration and processing have hampered commercialization of tar sands.

In the present commercial oil sands plants such as Syncrude and Suncor in Ft. McMurray, Alberta, strip or open pit mining has been used. This technique involves the removal of overburden and mining of tar sands using either bucketwheel excavators or draglines and transportation to the extraction plant by a series of long conveyor belts. Using the 'hot water' process developed by Dr. Karl A. Clark from the Alberta Research Council (Puttagunta et al., 1977), the bitumen is then extracted and upgraded. The remaining sand is sent to the tailings disposal. Storage of the tailings poses a major problem for a surface mine operation.

The oil sands formations range up to 60 meters in depth with overburden depths up to 700 meters (Humphreys et al., 1977). The oil content of the sand and the thickness of the

overburden limit the depth of the deposit for which strip mining techniques can be used economically. At present, only 10% of the reserve is considered mineable by surface methods (Baughman, 1978). Recovery of the remaining oil sands deposits will require either subsurface mining or in-situ techniques.

The principle of in-situ methods is to remove the bitumen only, thus eliminating some of the problems encountered in the disposal of sand. Of these methods, present studies have centred around forward/reverse combustion and steam injection. Both methods have undergone pilot scale testing in Alberta (Puttagunta et al., 1977), but the steam injection method has received the most attention and is considered to be exploitable in the near future. In this method, high pressure steam is injected into a central well. The addition of heat through this method into the oil sands formation lowers the bitumen viscosity. This enables the bitumen to be pumped from a group of producing wells surrounding the central one.

In order to optimize the extraction of oil, it is highly desirable to obtain good communication between the central and producing wells. One method for accomplishing this is to pump a liquid under high pressure into the formation in an attempt to produce horizontal fractures. However, factors such as the orientation of bedding planes and in-situ stresses result in a poor success rate with this method. A well is defeated when vertical fractures to

formations above or below the deposit are created. Hence a controlled method, such as introducing a high pressure water jet to produce a series of horizontal holes radiating outward from the well bore is of special interest. This method could be used to direct the fracturing process in establishing a better communication between wells. In so doing, the injection wells can be placed further apart providing an economic advantage. Other possible applications of this method include shaping electrodes for electrical heating and increasing the available surface area in the bore-hole for better heat transfer.

The capability of a high speed water jet to fracture and penetrate substances like rock and coal has been amply demonstrated (see for example Singh et al., 1974, Erdmann-Jesnitzer et al., 1980). In order to investigate the feasibility of jet cutting in oil sands, a correlation relating the depth of cut to jet parameters is required. However, little information pertaining to the depth of penetration of water jets in oil sands is available. Some earlier laboratory studies and field tests to determine a correlation have been carried out by Gilpin and Gates (1981). From the laboratory investigation, a correlation relating the depth of penetration to jet parameters (nozzle diameter and dynamic pressure) and total jetting time was developed. The results predicted by this correlation agreed closely with those of the field test. However, neither the correlation nor the field test provided sufficient

information to predict the ultimate depth of the penetration or the cutting time. Both of these quantities are important for evaluating a jet cutting operation.

In an attempt to obtain estimates for the ultimate depth of penetration, some test results of the characteristics of unconfined water jets by Yahiro et al. (1980) were incorporated into the first model (Gates and Gilpin, 1982). Yahiro et al. measured the average centerline pressure of a high pressure water jet as a function of the distance from the nozzle for various exit conditions. These exit conditions were: water jet into air, water jet into water, and water jet with a concentric air jet into water. Using the criterion that no cutting of oil sands occurs when the jet dynamic pressure at the nozzle falls below 1.2 MPa for standoff distances greater than 100 nozzle diameters (Gilpin et al, 1981), three estimates of ultimate depth were obtained. The field data were compared with these predictions and it was found that the field data fell below the curve for the water jet into air but above that for the concentric air water jet into water (Gates et al., 1982). It appears then, that the maximum depth probably lies between the curve for a water jet into air as an upper bound and that for a concentric air-water jet into water as a lower bound. A comparison between these estimates based on the lower bound and two cutting theories (Crow (1973), Hashish and duPlessis (1978)) was also carried out (Gates et al., 1982). The results of the comparison is demonstrated in

figure 1.1. From this figure, it can be seen that Crow's theory substantially underpredicts the maximum depth of penetration and also shows a linear dependence upon pressure while the actual case is nonlinear. A better agreement with the experimental data was found with the theory of Hashish and duPlessis by adjusting a parameter Cf which is a hydrodynamic coefficient of friction. However, the cutting theories were developed for a traversing jet rather than a stationary one and extension to the stationary jet case is questionable.

1.2 Present Investigation

As can be seen from the above discussion there is no theoretical method or sufficient experimental data from which a prediction of the ultimate depth of penetration can be made. It is desirable then to have results similar to those of Yahiro et al. for a confined jet as this would provide a more realistic model of the actual situation than an unconfined jet. To this end an experimental apparatus was built to simulate a confined jet in a down-hole jetting geometry. The flow of the jet was investigated qualitatively by flow visualization and quantitatively by measuring the pressure of the jet on a simulated cutting face. From this experimental data an empirical model to predict maximum depth of penetration and cutting rates was developed. The predictions of this model were then compared to some limited field test data and to a correlation based on Gilpin (1981).

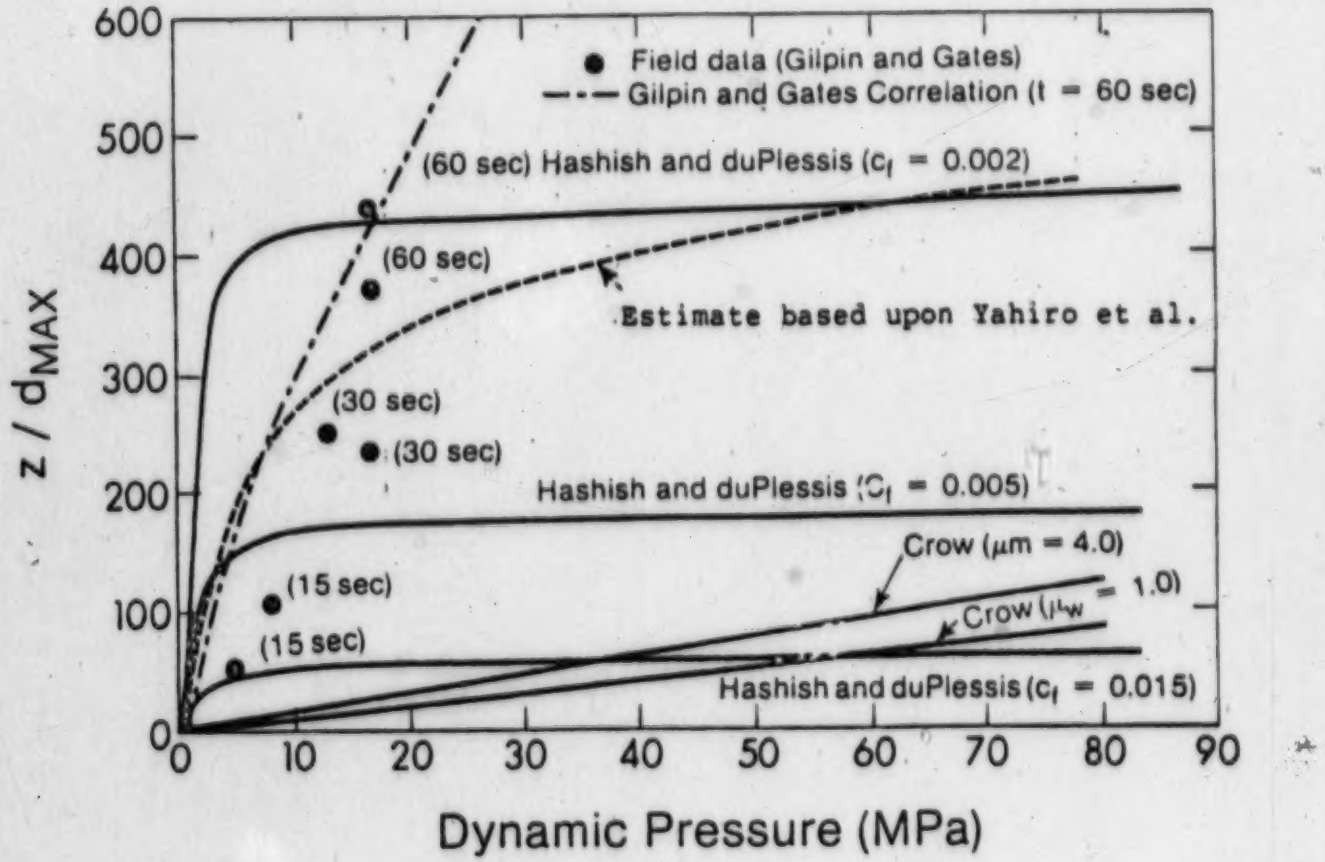

Figure 1.1 Comparison of predictions of the ultimate depth of penetration for an unconfined jet (after Gilpin & Gates, 1982).

2. Experimental Apparatus and Procedures

2.1 Apparatus

A laboratory model was constructed to simulate a down-hole jet cutting geometry like that of figure 2.1. The experimental apparatus is shown schematically in figure 2.2 and a photograph of the apparatus is provided in plate 2.1. The model consists of a vertical and an horizontal section supported in a steel tubing frame. The test model was constructed with plexiglass in order to study the flow visually.

The vertical section consists of a 0.3 meter square tube, 2.5 meters high which is open at the top and closed at the bottom. Drainage of the spent water at the bottom of this vertical section was controlled by two valves. A square window of 0.2 meter was constructed on one side of the vertical section to provide access to the nozzle assembly.

The horizontal section representing the hole pierced by the water jet was modelled by a circular tube. Because the size of the actual hole produced for given jetting conditions is not known several sizes of tubing were used ranging from 38 mm to 102 mm in diameter. A moveable piston carrying a load cell slides along the length of the tubing simulating the depth of the hole cut. The piston is connected to a long tubular rod which is held against the frame using a tapered clamping device. Hence, the piston can

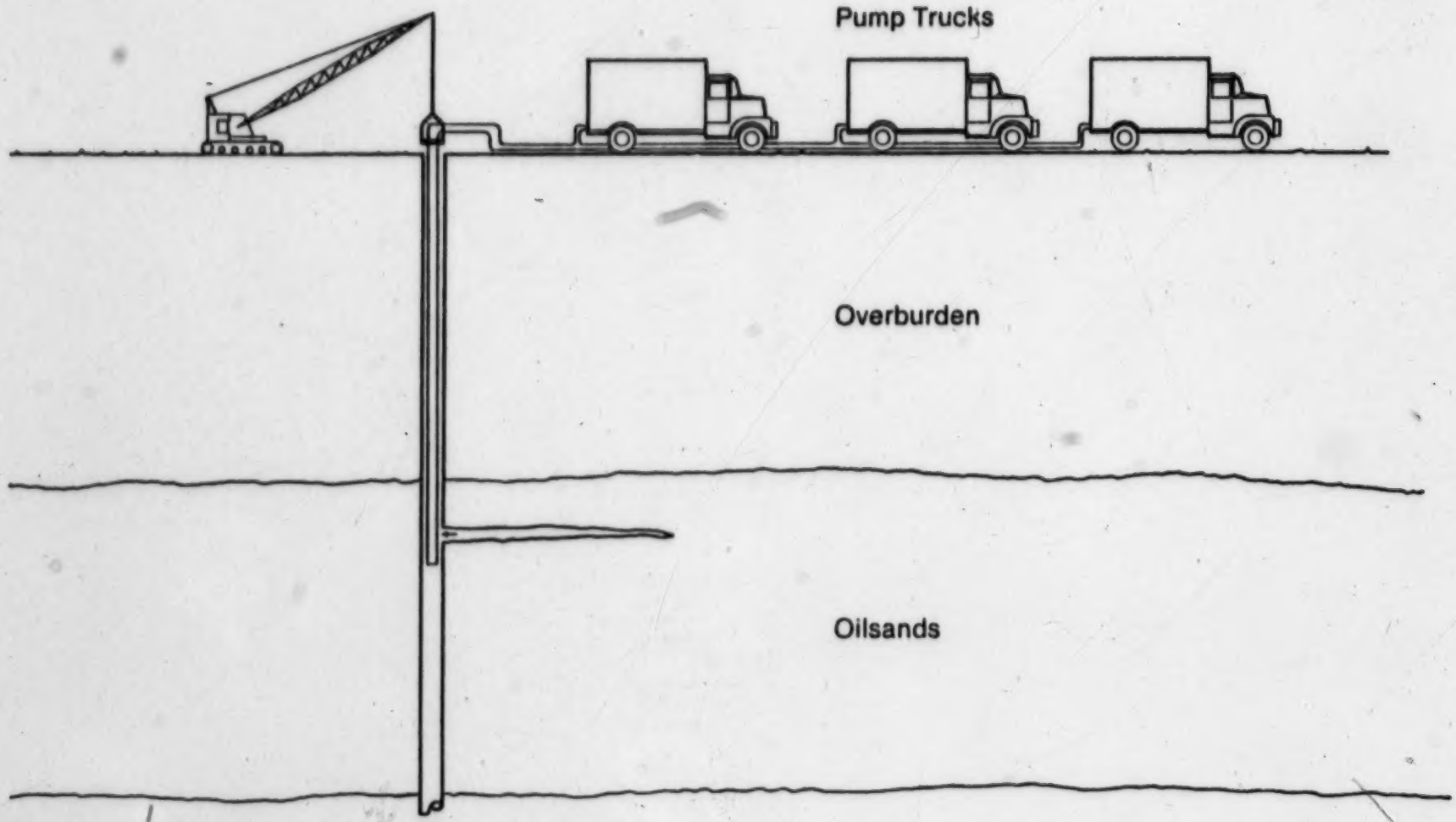

Figure 2.1 A schematic drawing of a proposed down-hole jet piercing operation.

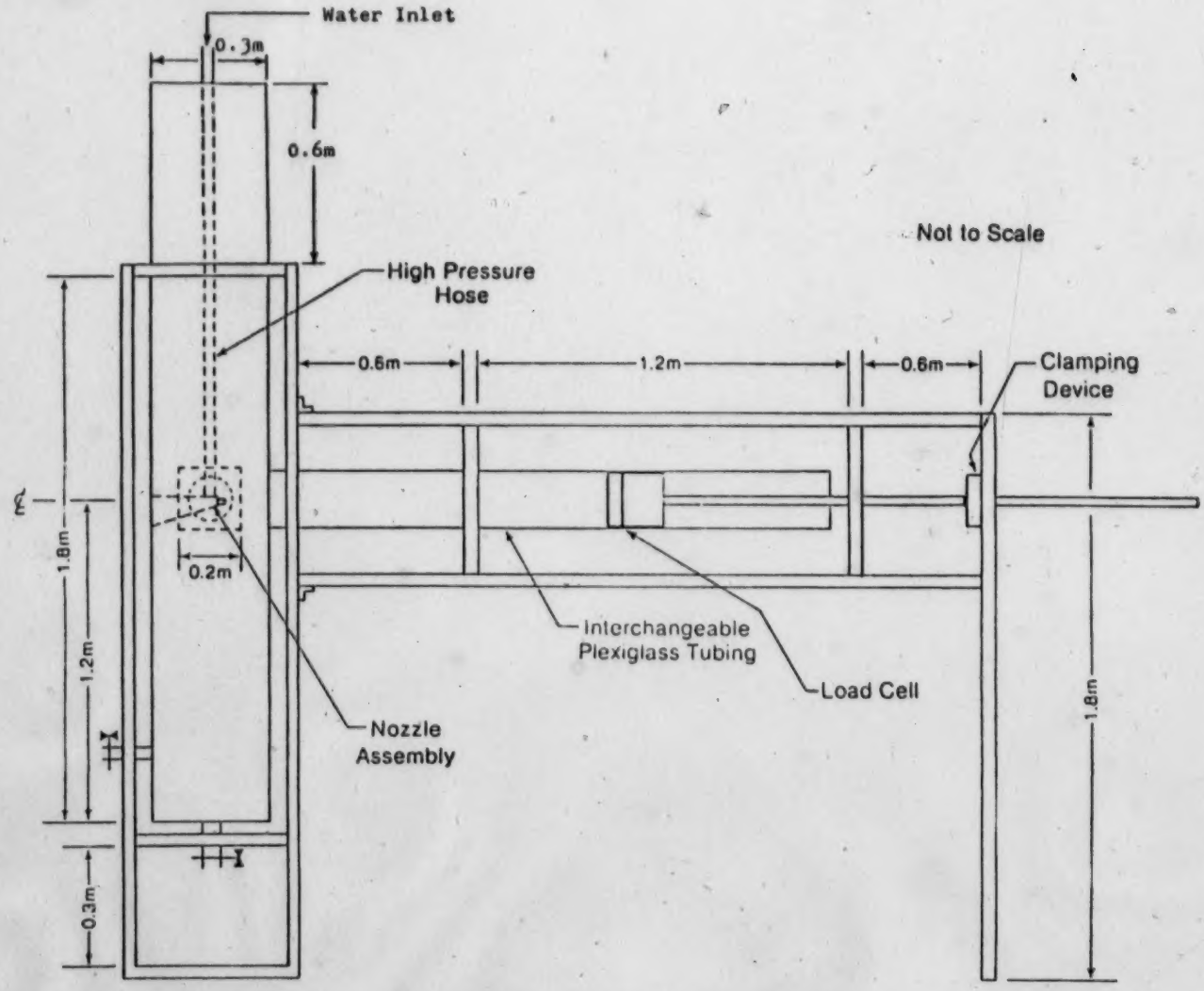

Figure 2.2 A schematic diagram of the laboratory model of a down-hole jet piercing geometry.

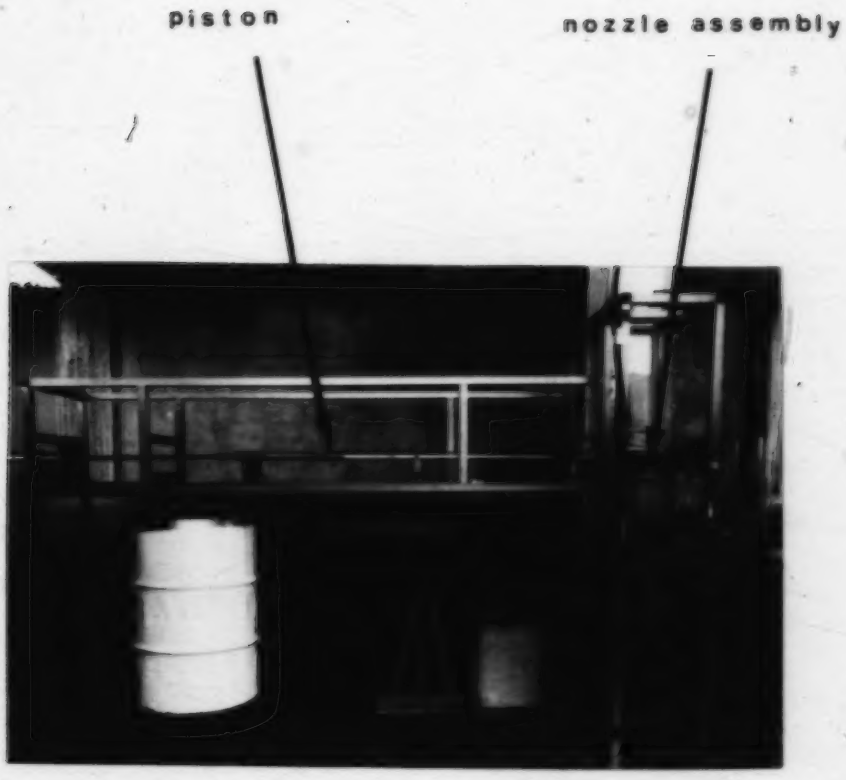

Plate 2.1 A photograph of the experimental apparatus used to model a down-hole jet piercing geometry. In this photograph a 38 mm diameter horizontal tube is in place and the piston to nozzle distance is 0.9 meter.

be fixed at any position along the tube.

In addition to the solid walled tubes, some experiments were carried out using a porous walled tube. The motivation for these tests came from field test observations (Gilpin and Gates, 1981) in which it was noted that spent water returned through previously drilled holes and cracks in the oil sands formation. Consequently, the assumption of a solid wall appears to be too severe. To simulate the porosity, a large number of holes were drilled in a 51 mm diameter tube. Five percent of the total surface area of the tube was drilled out uniformly over the entire length of the tube, with holes of 6.35 mm in diameter. A 0.2 meter square box was built to enclose the porous tube to prevent splashing of the water when the porous test was done. Spacers supported the porous tube inside this box. This box was open at the back allowing the water to drain away. This arrangement can be seen in plate 2.2.

A high pressure three cylinder positive displacement pump driven by a 30 kW electric motor generated a pressurized flow of water which was conducted through a flexible hose to the nozzle assembly. The volume flow rate of the water was determined from the rotational speed of the pump. Pump speed was measured utilizing a magnetic sensor and a magnet attached to the hub of the pump drive pulley. The resulting pump calibration curve is shown in figure A.1 in the appendix.

Plate 2.2 A photograph of the apparatus arranged for porous wall tube tests. The square horizontal box enclosing the porous tube collects the water escaping through the pores.

2.2 Nozzle Assembly

The nozzle assembly mounted in the vertical section opposite the horizontal tube was designed to absorb the high thrust force of the jet and to allow for fine adjustment of the nozzle position and direction. This assembly, using several set screws and washers, was capable of adjusting the jet in three degrees of freedom: yaw angle and vertical and horizontal displacements. A photograph of this assembly can be seen in plate 2.3.

2.3 Nozzle Geometry

The nozzles used in this experiment were made of stainless steel with a tungsten carbide insert. As no information pertaining to the geometry of the nozzle was available from the manufacturer (Hydro Manufacturer Inc.), the internal geometry of the nozzle was determined by taking a mold with ERTV molding rubber. This molding has a volume shrinkage of less than one percent. The nozzle profile was then determined by placing the hardened mold in a shadowgraph and recording the profile coordinates. The nozzle profile is shown in figure 2.3.

2.4 Instrumentation

2.4.1 Load Cell

To measure the pressure that the water jet exerts on a material surface, a load cell was constructed and mounted in

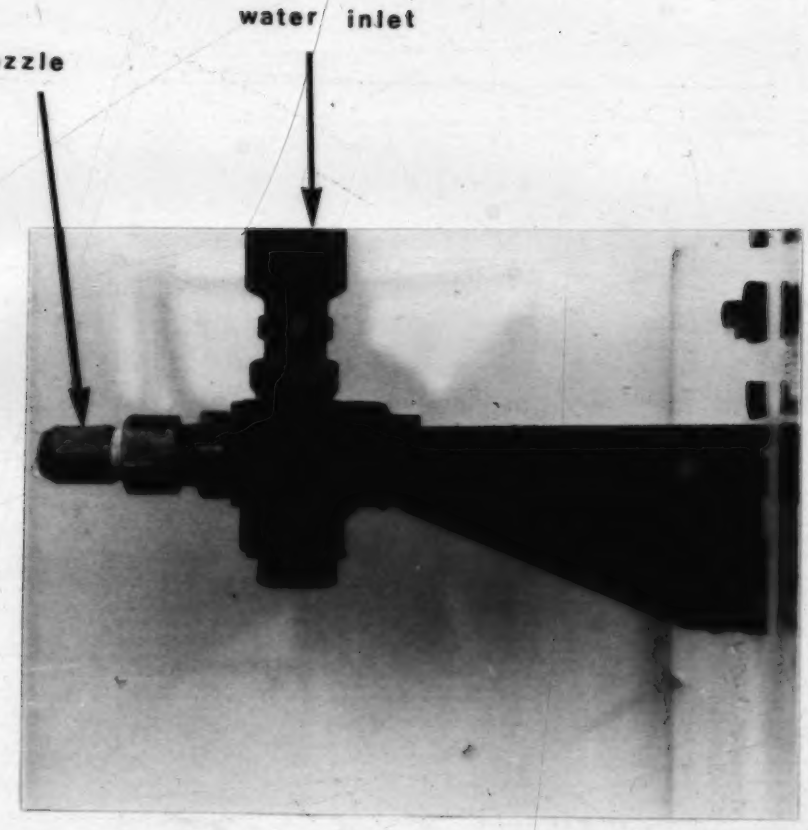

Plate 2.3 A photograph of the nozzle support and alignment assembly.

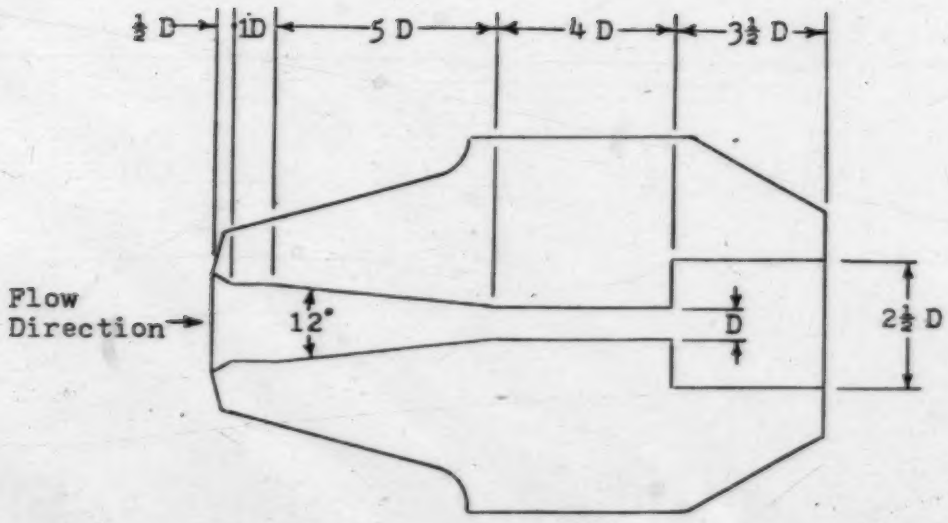

D: Nozzle diameter

Figure 2.3 A schematic diagram of the nozzle geometry.

the piston surface. All the pistons were made to accommodate the same load cell. The piston and load cell arrangement can be seen in plate 2.4.

The load cell is a 25.4 mm diameter by 2.54 mm thick steel diaphragm with a 6.4 mm rim as shown in figure 2.4. Foil strain gauges were mounted on the side of the diaphragm that was not exposed to the water. Four gauges were used to give a full bridge configuration. The arrangement of the gauges, similar to Werner (1953) as shown in figure 2.4, provided temperature compensation. With a uniform pressure applied to the diaphragm, the middle gauges (2 and 3) are subjected to tension while the outer gauges (1 and 4) sense compression. The strain measured from these gauges is directly proportional to a uniform pressure applied to the diaphragm. An experimentallly measured value of the first resonant frequency of the plate showed a value of 20 kHz. This was done by dropping a small ball bearing onto the middle of the load cell and observing the trace of the strain gauge bridge output on an oscilloscope.

The load cell was statically calibrated at room temperature with compressed air as shown in plate 2.5. The relationship between the applied pressure to the measured electrical output is shown in figure A.2 in the appendix.

2.4.2 Signal Analysis

A schematic diagram of the load cell signal analysis procedure is shown in figure 2.5. The signal obtained from

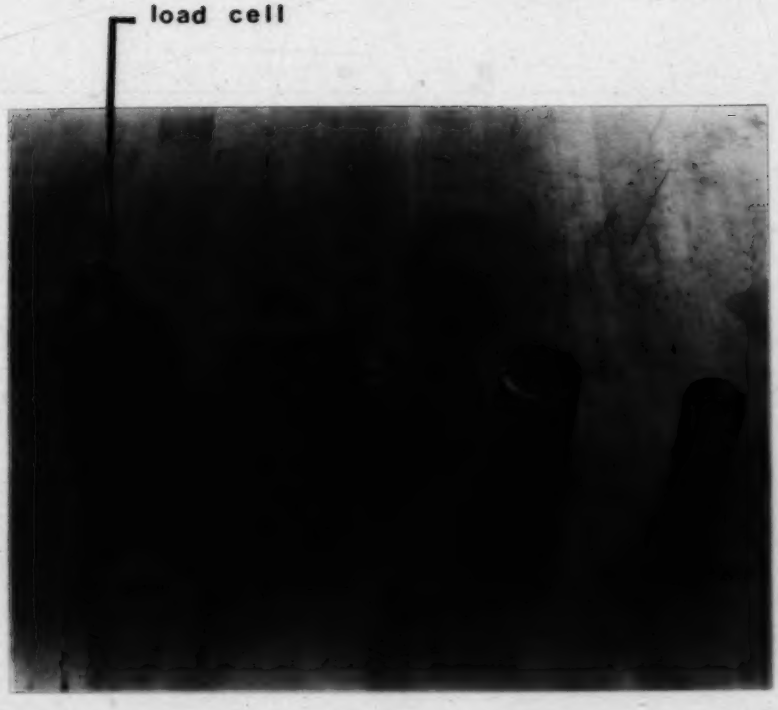

Plate 2.4 A photograph of the four pistons used in these experiments. Also shown is the load cell about to be mounted in the 102 mm piston.

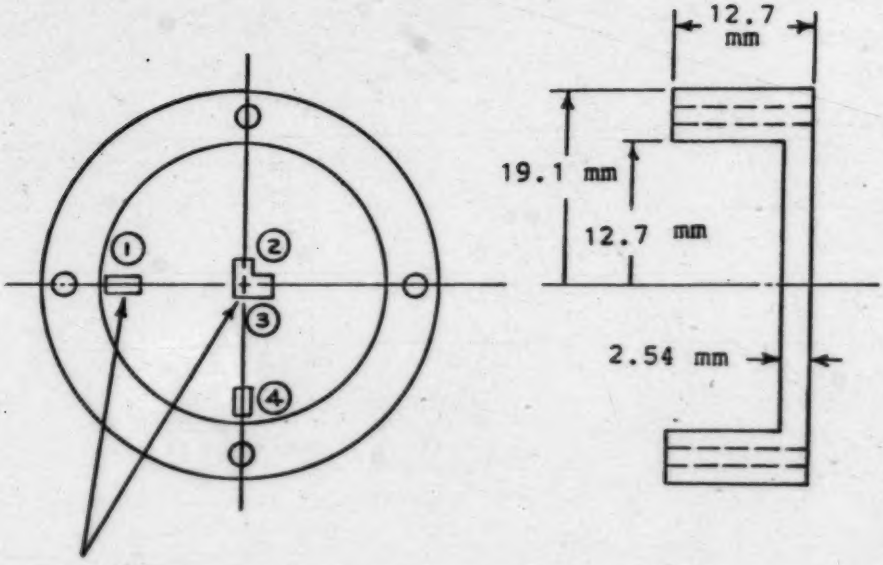

350 Ω Strain gauges

Gauge factor 1 & 4 : 2.084
2 & 3 : 2.12

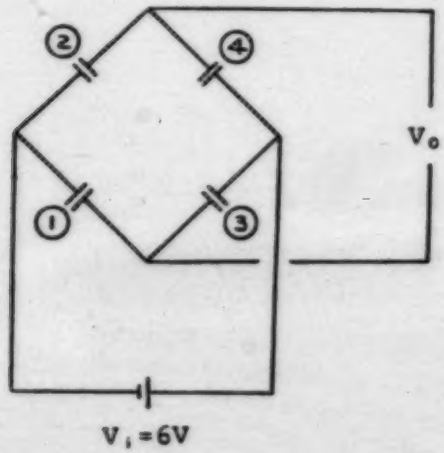

Figure 2.4 A schematic diagram showing the load cell geometry and the positioning of the strain gauges.

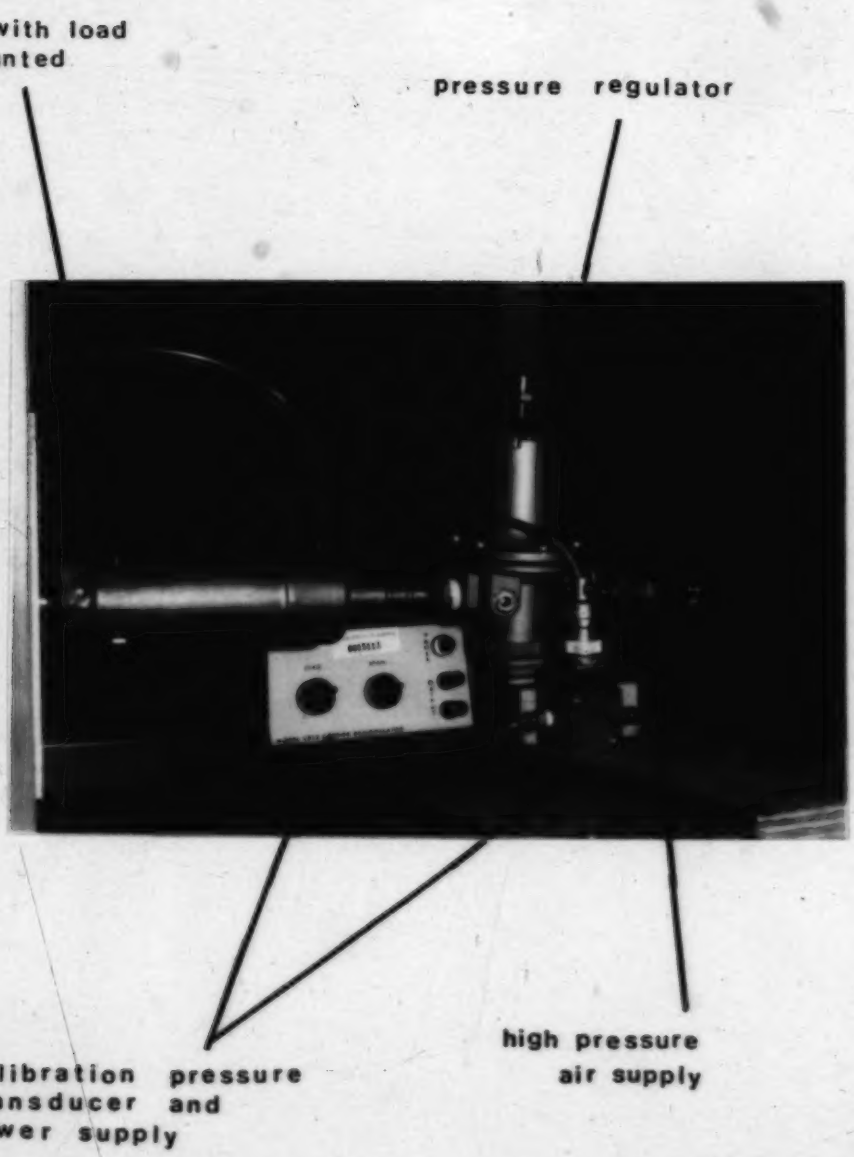
piston with load cell mounted
pressure regulator
calibration pressure transducer and power supply
high pressure air supply

Plate 2.5 A photograph of the apparatus used to calibrate the load cell.

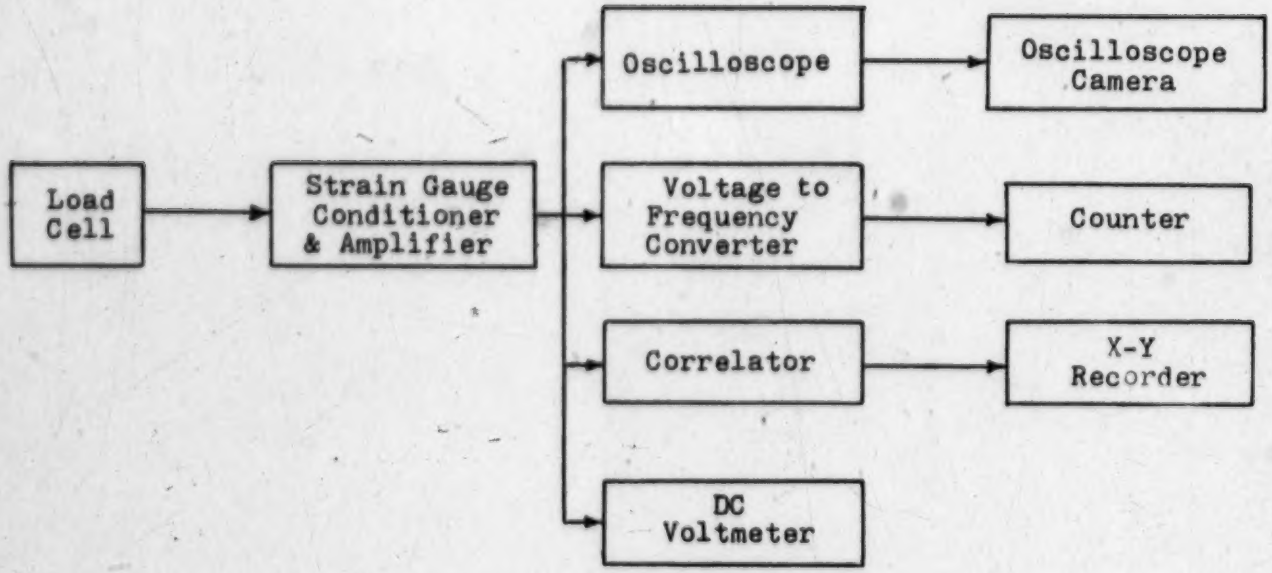

Figure 2.5 A block diagram summarizing the stages in the analysis of the load cell signal.

the load cell after amplification had a very large fluctuating component and a small steady offset. A sample trace of the signal from the oscilloscope is shown in plate 2.6. Because of the nature of the pressure signal, it seemed more appropriate to examine the signal in more detail than only recording peak and average values. The discrete nature of the signal suggested that the impact of the water jet could be viewed as a stochastic process. The pressure signal is therefore analyzed to provide a frequency of occurrence distribution. This was accomplished by recording the signal with an HP 3721A signal correlator to provide the frequency and cumulative frequency distributions. From frequency distribution, the probability density function is determined by normalizing the frequency distribution to produce an area under the curve of one. The area underneath the probability density function is known as the cumulative density function, and gives the probability that a signal is below or above a certain amplitude.

The pressure signal was sampled at a rate of 3 kHz (the fastest available), and each sample is placed into a bin according to its magnitude. In probability density measurements the sampling sequence stops when the number of samples in any one bin reaches a pre-set number (in the present case, 32x1024). In the probability integral measurements, processing ceases after about 4 times this number of samples have been taken.

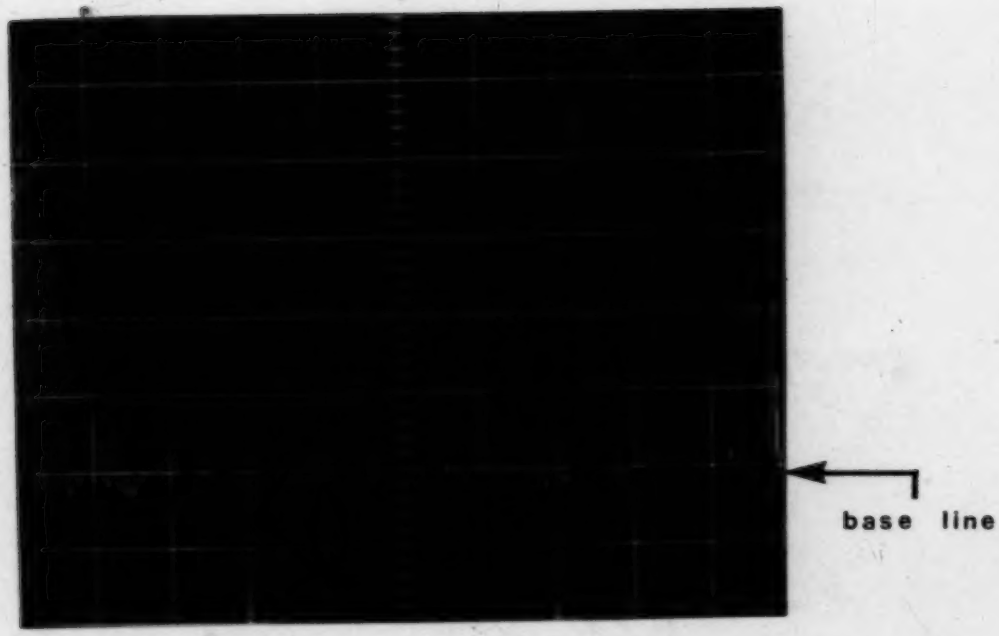

Plate 2.6 An example oscilloscope trace of the load cell signal.

Vertical scale: 50 kPa/cm
Horizontal scale: 5 millisec/cm
Nozzle diameter: 1.6 mm
Nozzle pressure: 10 MPa
Standoff distance: 0.5 meter

In addition to the frequency distribution the average value of the signal was also measured. This was done using a voltage to frequency converter and a counter. The input pressure signal was converted to frequency and the average frequency was then obtained over a fixed time interval (10 seconds).

2.5 Test Procedure

At the beginning of each test the tubing was levelled and the jet was centered by adjusting the set screws in the jet assembly so that the jet hit at the center of the face of the load cell. It was then assumed that the jet hit the center of the face of the piston along the length of the tube. The jet offset due to gravity was estimated to be approximately 0.2 mm for a standoff distance of 1 meter.

Before any readings were recorded, the load cell was checked for seating by running the pump on and off several times. In doing this, the load cell would be properly seated and the bridge could be balanced. Subsequently, any strain measured would be due to the pressure of the water jet. The water temperature for all the experiments was kept constant at 22°C.

During the test, for a given nozzle diameter, tube diameter and flow rate, the average pressures for each standoff distance were obtained. Plots of probability and cumulative density functions from the correlator were also recorded. To prevent damage to the load cell, the minimum

standoff distance was kept at 31 cm. The load cell was recalibrated regularly, particularly after running the smallest nozzle diameter because of its high pressure, and whenever a new piston was used. This was done to ensure no permanent deformation of the diaphragm resulted from the previous run and the same calibration curve could still be used.

3. Presentation of Results

For a given nozzle diameter, dynamic pressure and tube size, plots of probability and cumulative frequency distributions were recorded for each nozzle to piston (standoff) distance. In addition average pressures were recorded. The range of variables used were:

A. Solid wall

Nozzle sizes: 3.2 mm, 2.4 mm, 1.6 mm.

Tube dia. : 102 mm, 76 mm, 51 mm, 38 mm.

Pressures : up to 35 MPa.

Standoff distance : 0.3 m to 1.6 m.

B. Porous wall

Nozzle sizes: 3.2 mm, 2.4 mm, 1.6 mm.

Tube dia. : 51 mm.

Porosity : 5%.

Pressures : up to 35 MPa.

Standoff distance : 0.3 m to 1.7 m.

In addition to making quantitative measurements of the pressure the water jets were also studied qualitatively by flow visualization. Since the flow observations are very useful in interpreting the quantitative data, they shall be presented first.

3.1 Flow Visualization

The flow visualization was accomplished by high speed photography. A high speed movie camera (HYCAM) was used to record the flow of the unconfined and confined jets. The camera, running at 5000 frames per second, was positioned perpendicular to the jet center-line at a point 0.5 meters from the nozzle. Illumination was provided by tungsten lamps. From these flow observations it could be seen that several distinct flow regimes could be defined. These are:

1. Unconfined jet.
2. Confined jet with solid wall:
    a. no slug flow regime
    b. intermittent slug flow
    c. permanent slug flow.
3. Confined jet with porous wall.

The features of each of these flow regimes will now be described.

1. Unconfined jet.

Before examining the more complex features of the confined jet flow, the flow characteristics of an unconfined jet were investigated. A sequence of frames from the high speed movie for an unconfined jet is shown in plate 3.1. The direction of the water jet is from right to left. As can be seen from this series of frames, the jet has a definite structure that is repeatable. The basic structure is that of a "slug" or "packet" of water trailed by a large number of small

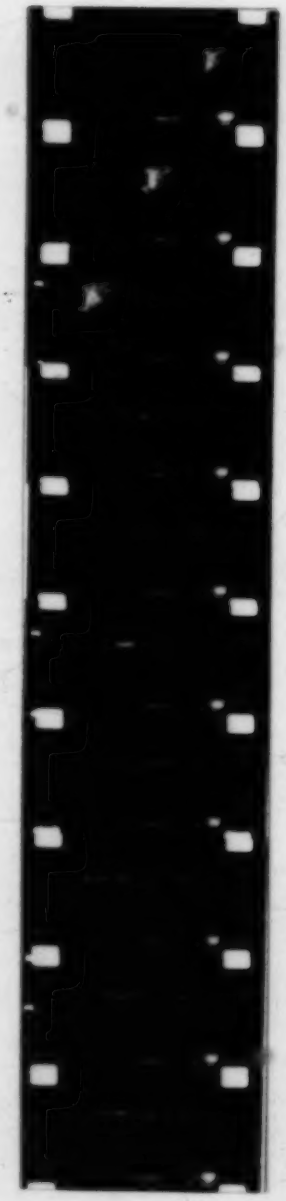

Direction of flow is
from right to left

Nozzle diameter: 2.4 mm
Nozzle pressure: 2 MPa
Standoff distance: 0.5 meter
Width of frame: 28 cm
Time between frames: 2 milliseconds

Plate 3.1 A sequence of high speed camera frames showing the flow of an unconfined continuous jet.

droplets. The reason for this structure and its repeatibility can be traced to the manner in which the jet is produced.

Recall that the jet is produced by a positive displacement pump having three pistons. On each discharge stroke as the piston moves from bottom dead center to top dead center its speed varies from zero to some maximum value and then back to zero. Consequently a similar speed variation occurs in the water jet as it leaves the nozzle. The high speed water produced near mid-stroke very rapidly overtakes the slower moving portion of the jet produced at the beginning of the stroke forming a "slug" or "packet" of water. The slower moving portion of the jet produced near the end of the jet trails even further behind the slug in a series of small droplets.

This modulation of the water jet was clearly shown by a spectral analysis of the pressure signal and correlated exactly with the pump rotation rate.

2. Confined jet with solid wall.

Observations of the flow when the jet was confined within the solid wall tubes suggested that the flow be divided into three regimes. These are:

a. No slug flow regime.

In this flow regime no interference occurs between the incoming jet and the spent water. The water jet hits the piston and flows radially across

the piston face towards the tube wall. As it hits the tube wall, the water jet turns 90 degrees and flows along the tube wall towards the incoming jet. At a small standoff distance, spent water returns along the tube wall concentrically to the incoming jet. As the standoff distance increases, the spent water from the upper part of the tube falls along the tube wall and joins the flow of spent water from the lower part of the tube. A sketch of the latter type of flow is provided in figure 3.1. This flow regime was found in the 76 mm and 102 mm tubes almost over the entire range of standoff distances.

b. Intermittent slug flow.

As the standoff distance is increased some interference between the spent water and the incoming jet occurs. This interference can be caused by either rapid spreading of the jet so that it contacts the tube walls or by large flow rate so that the spent water can not drain fast enough. The result of this interference was to cause a "hold up" of some of the spent water so that a slug of water forms in front of the piston. The presence of the slug at this stage is not continuous, but depends upon which portion of the jet is impinging on the piston. A sketch of the flow can be seen in figure 3.2.

c. Permanent slug flow.

As the standoff distance is increased further, the accumulation of the spent water from the intermittent slug flow increases to the point where the presence of the slug becomes continuous. At this point the incoming jet no longer strikes the piston surface directly, but instead is dissipated at the front or upstream face of the slug. Further increases in the standoff distance results in a lengthening of the slug with the upstream face remaining approximately in the same position. A sketch of the flow in this case is provided in figure 3.3.

3. Confined jet with porous tube.

The holes in the porous tube allow the spent water to drain from the tube preventing any accumulation of water at the piston face. The spent water flows radially from the piston towards the tube wall. Most of the water flowed directly out of the tube through the pores when it reached the tube wall. However, some of the spent water changed direction as it hit the wall and flowed towards the incoming jet. The pores permitted this spent water to drain from the bottom of the tube without ever reaching the vertical section. A sketch of this type of flow can be seen in figure 3.4.

Figure 3.1 A sketch illustrating the flow within the tube when no interference occurs between the incoming jet and the returning water.

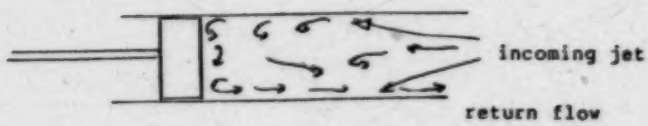

Figure 3.2 A sketch illustrating the flow within the tube when interference between the incoming jet and the spent water begins to occur.

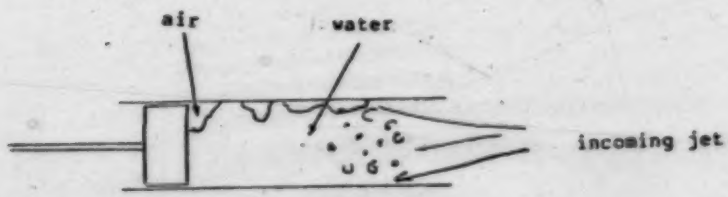

Figure 3.3 A sketch illustrating the flow within the tube when the presence of the slug has become continuous.

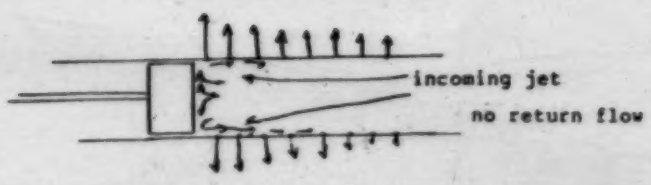

Figure 3.4 A sketch illustrating the flow within the tube of a porous wall.

3.2 Quantitative Results

3.2.1 Frequency distribution

Plots of the probability and cumulative density functions for various distances and sets of parameters were recorded on a X-Y recorder and later digitized. Some examples of these results are provided in figure 3.5 to 3.11. The results are recorded in Gates and Toogood (1983).

From figure 3.5 it can be seen that for small standoff distance the mean and variance of the probability density function are large. As the distance from the nozzle increases, the probability density function becomes narrower indicating a decreasing variance. The mean of the pressure signal also decreases as the standoff distance increases. This general trend is observed for smaller tube diameters as shown in figures 3.7 to 3.9. The shape of the probability density function for large tube diameters rises and drops off gradually (figures 3.5 to 3.7). However, for smaller tube diameters where the slug forms, the shape of the probability density function behaves differently as indicated in figures 3.8 to 3.9. The probability density function rises and drops off immediately without any gradual tailing off as observed in the non-slug case. The variance of this slug case is small. This is due to the fact that the slug of water acts as a cushion in front of the piston hence dampening any pressure fluctuations. For a higher dynamic pressure, the general trend of the probability density

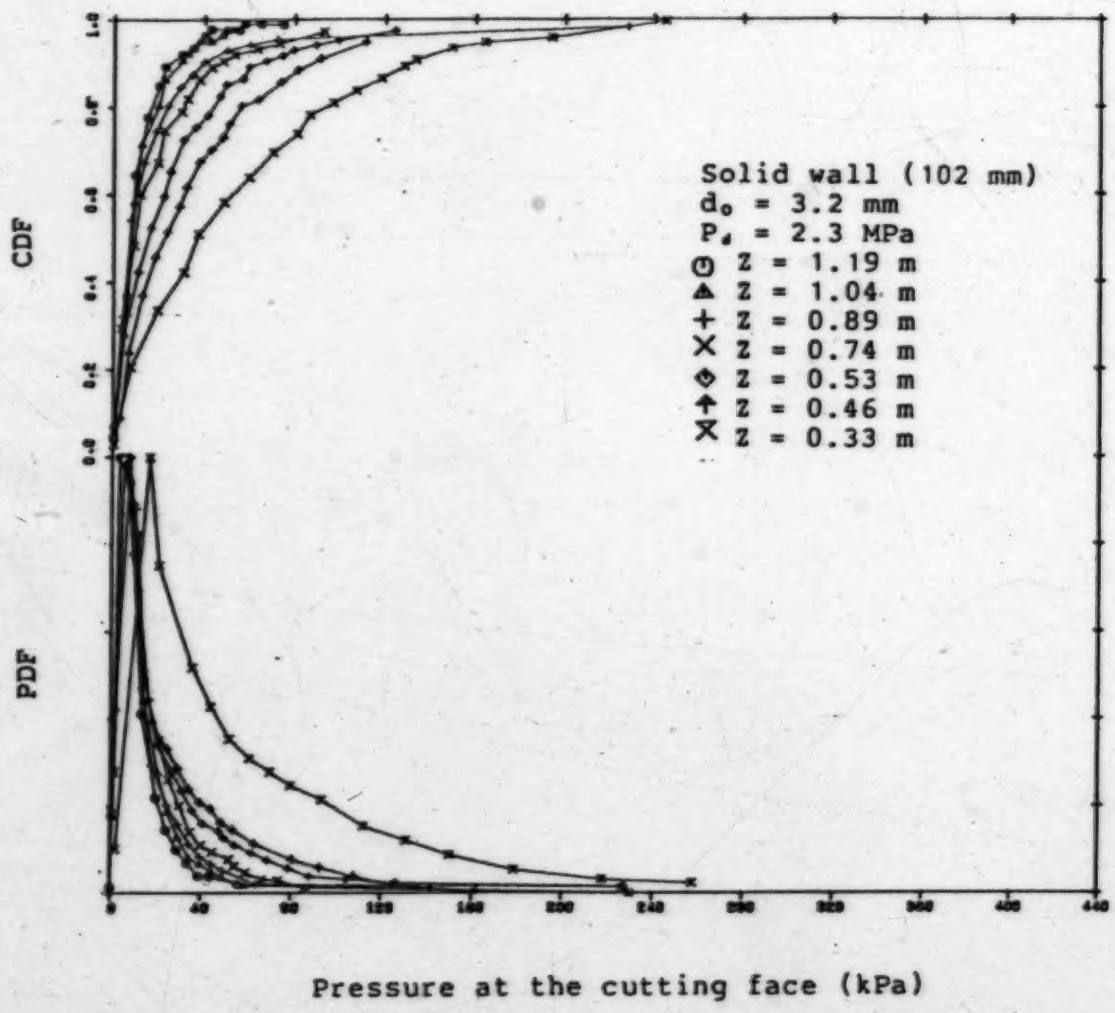

Figure 3.5 The probability and cumulative density function of the load cell signal for increasing values of the standoff distance (D=102 mm, P_d=2.3 MPa).

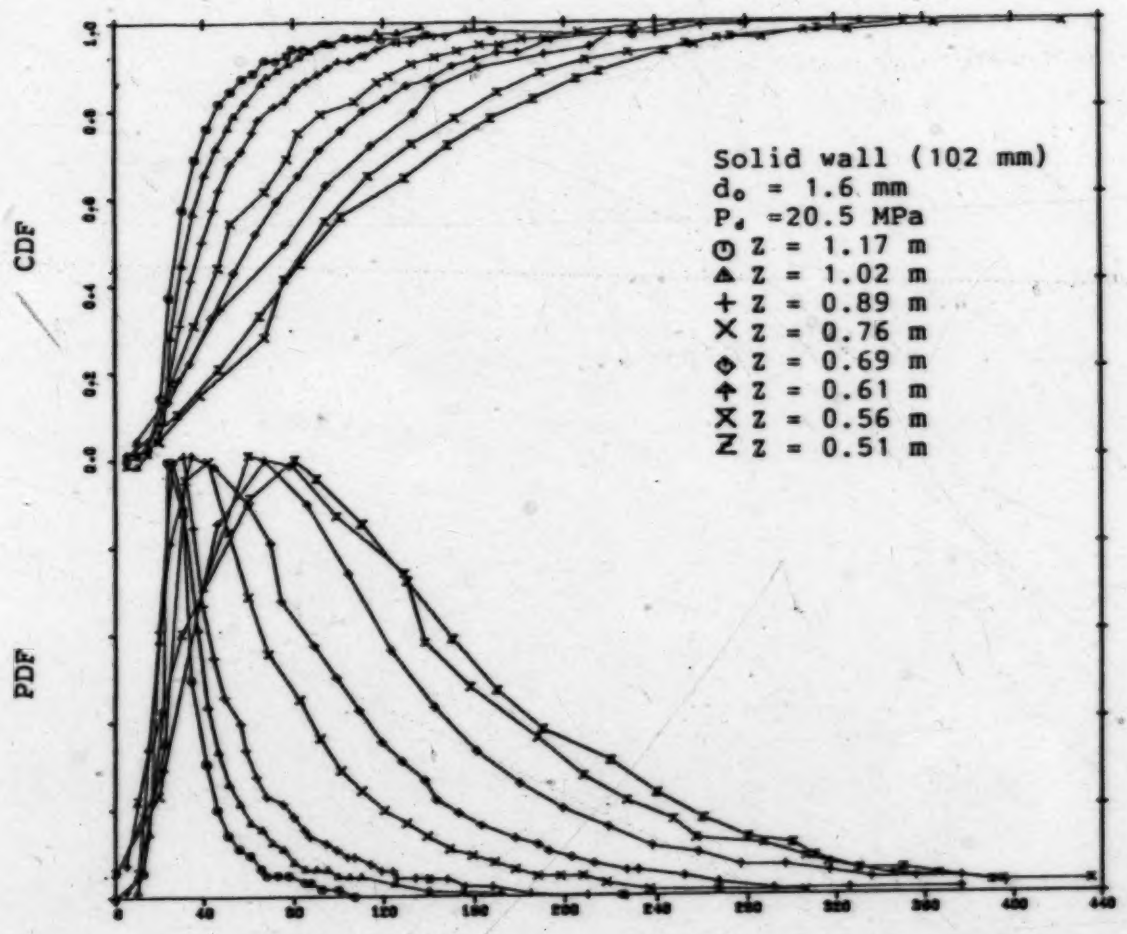

Figure 3.6 The probability and cumulative density function of the load cell signal for increasing values of the standoff distance (D=102 mm, P_d =20.5 MPa).

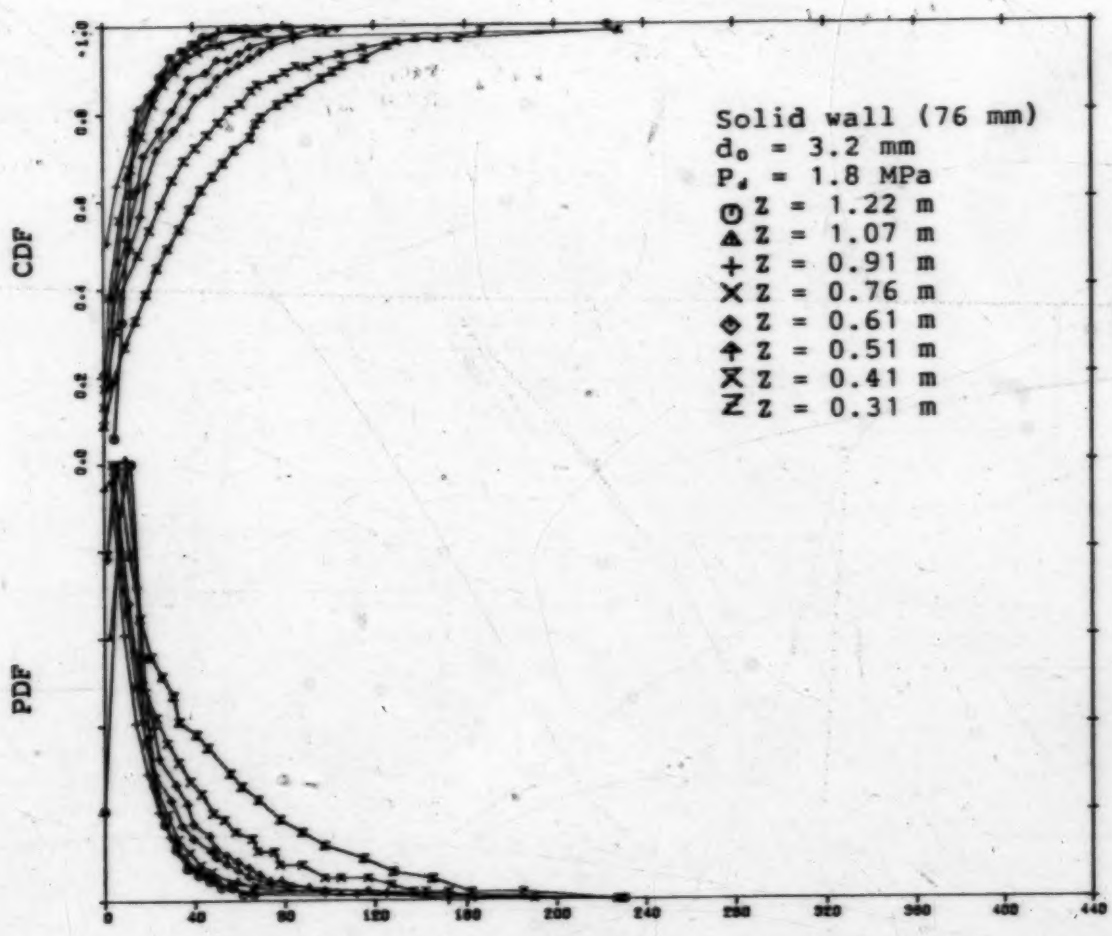

Figure 3.7 The probability and cumulative density function of the load cell signal for increasing values of the standoff distance (D=76 mm, P_d =1.8 MPa).

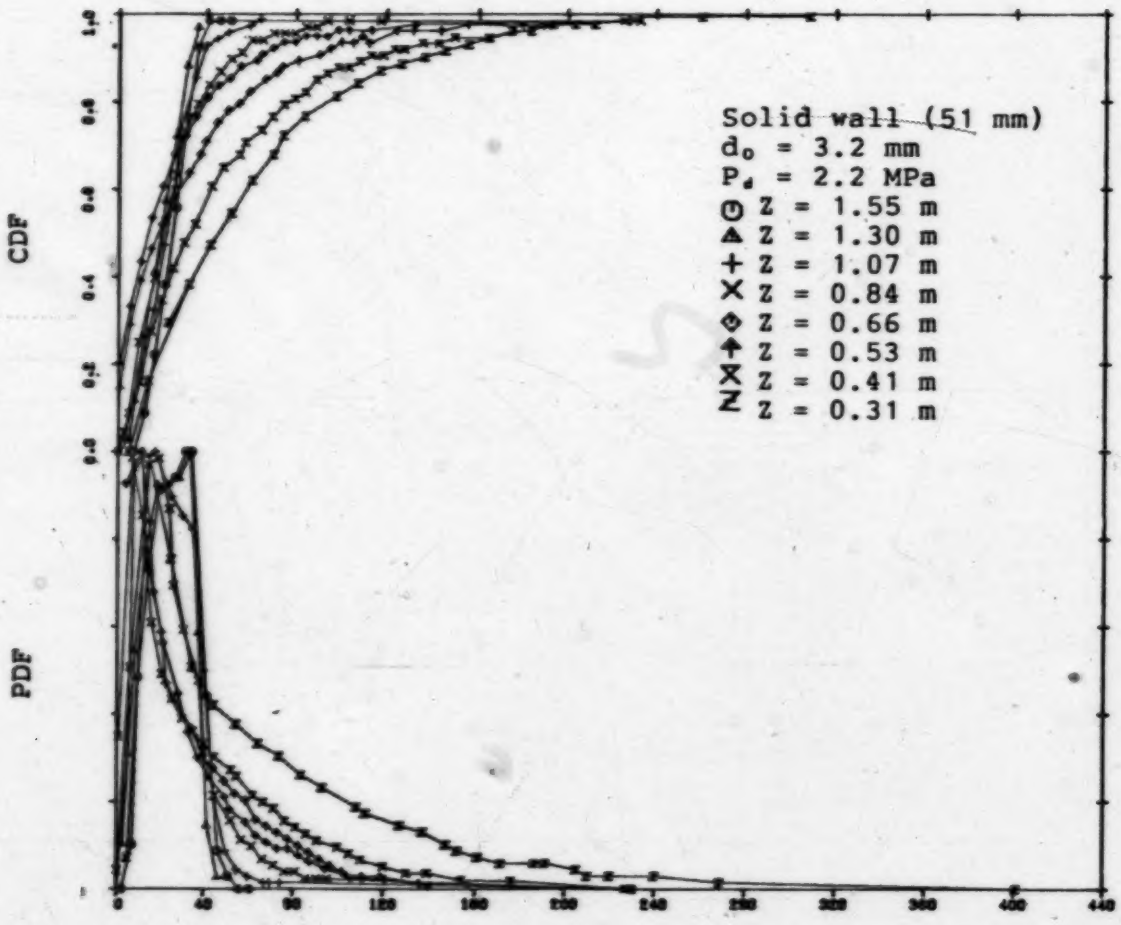

Figure 3.8 The probability and cumulative density function of the load cell signal for increasing values of the standoff distance (D=51 mm solid, P_d =2.2 MPa).

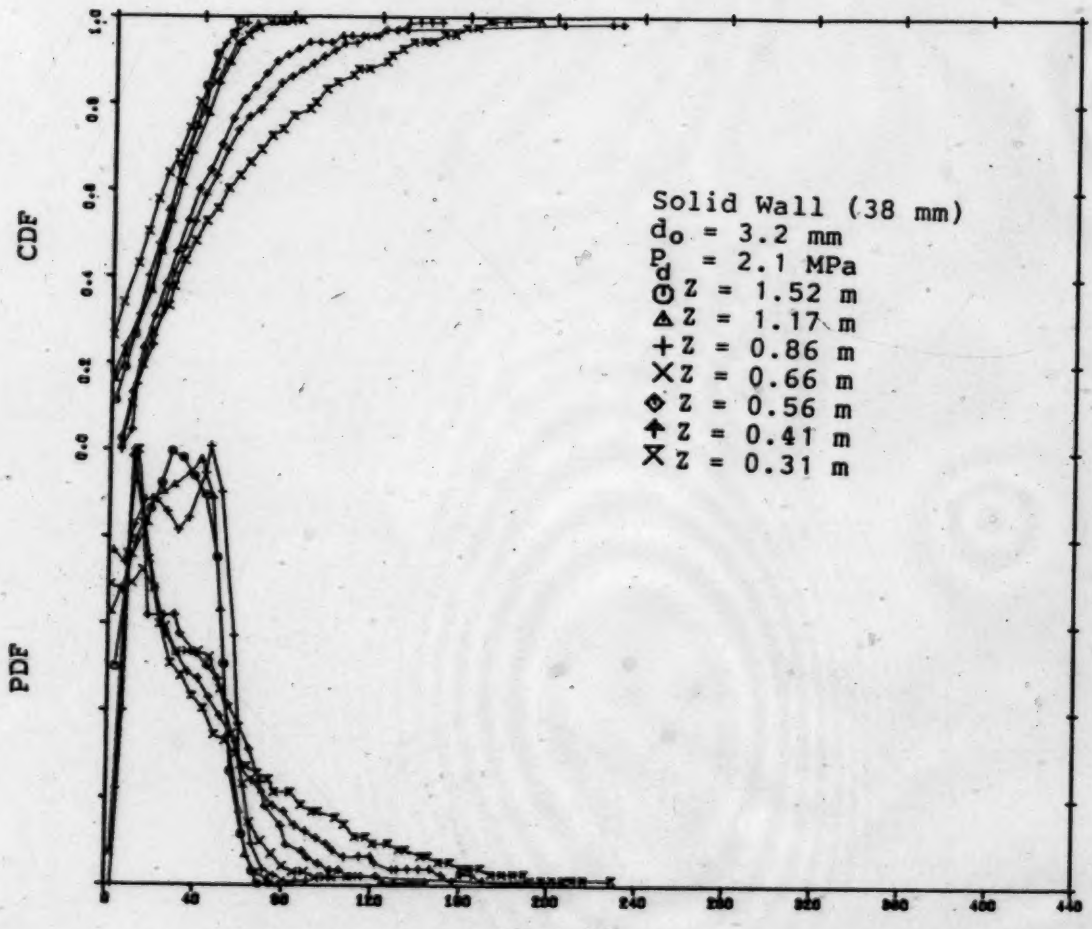

Figure 3.9 The probability and cumulative density function of the load cell signal for increasing values of the standoff distance (D=38mm, P_d=2.1 MPa).

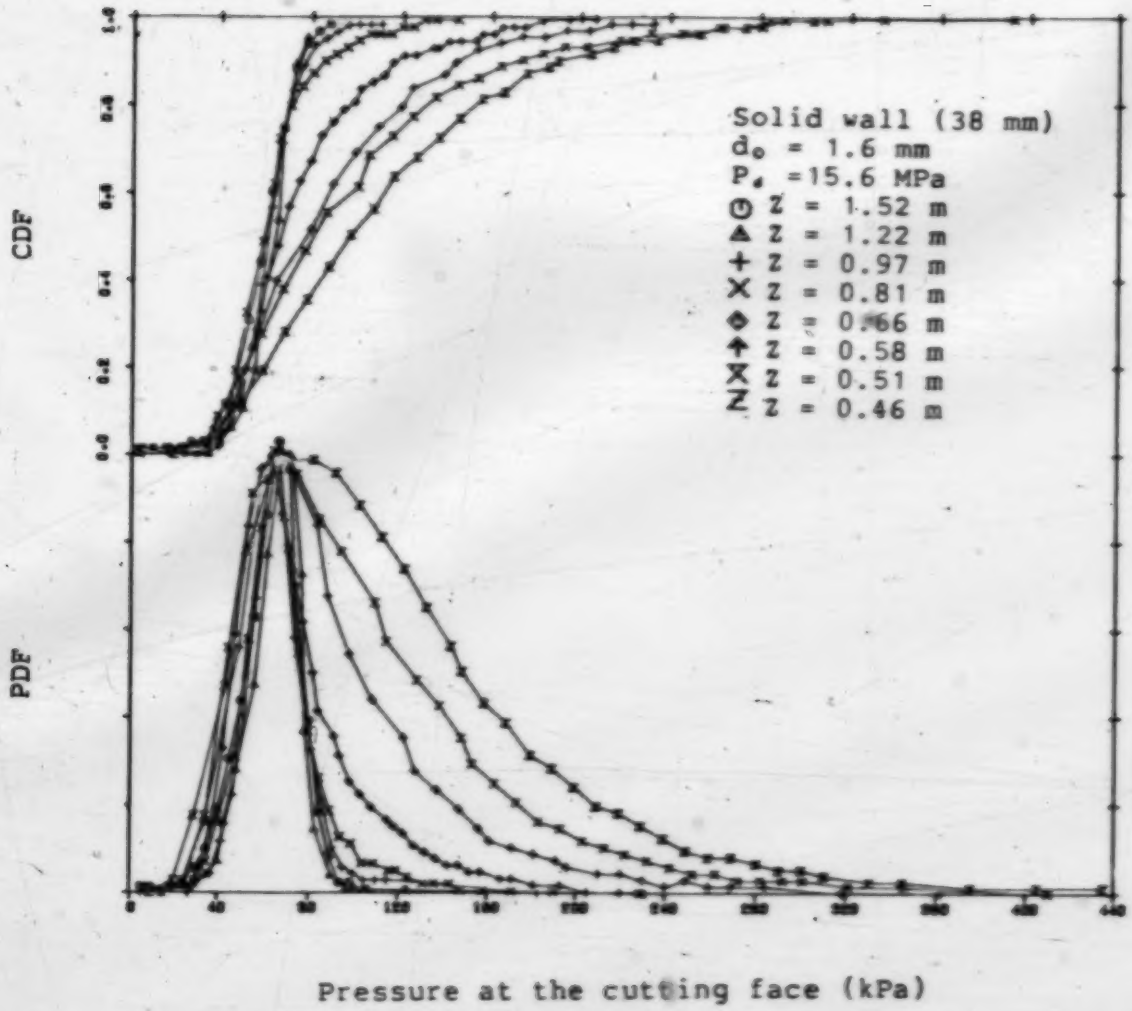

Figure 3.10 The probability and cumulative density function of the load cell signal for increasing values of the standoff distance (D=38 mm, P_a =15.6 MPa).

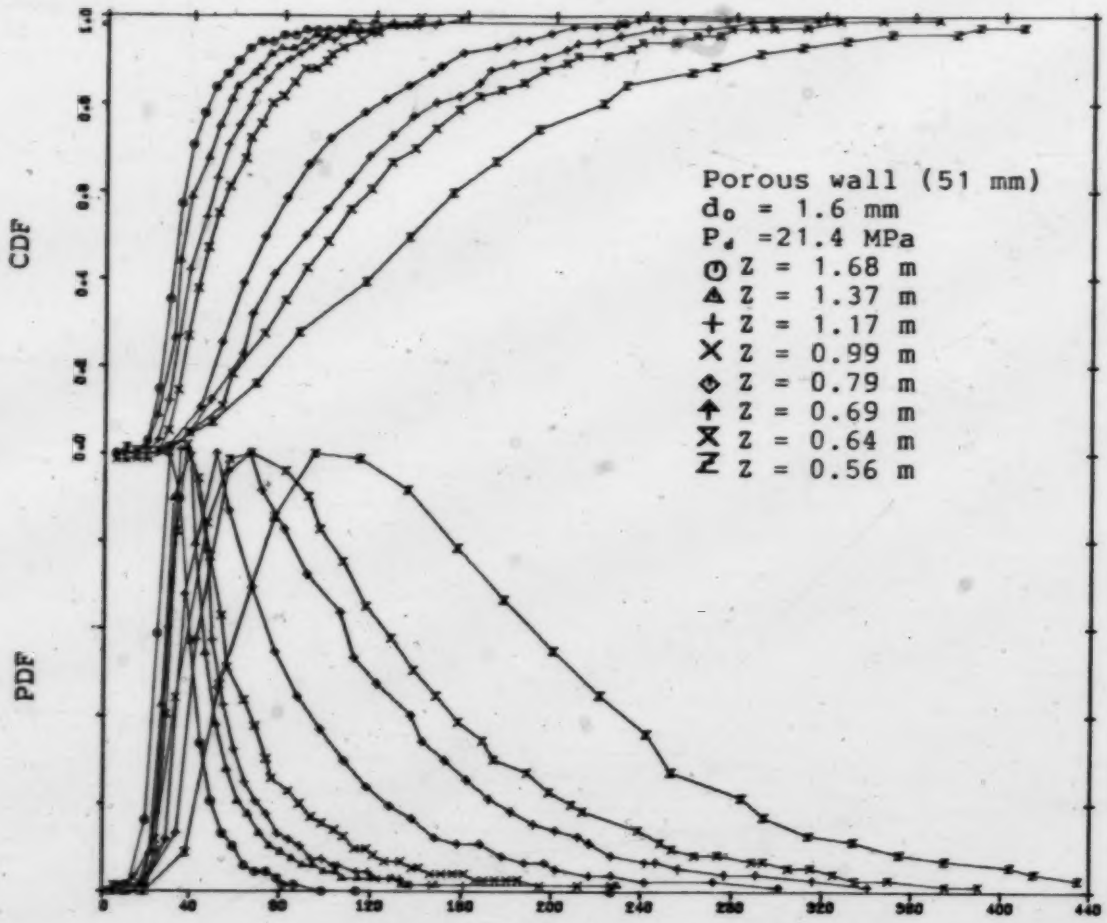

Figure 3.11 The probability and cumulative density function of the load cell signal for increasing values of the standoff distance (D=51 mm porous, P_d =21.4 MPa).

function still holds. That is as the distance from the nozzle increases, the variance and mean of the pressure signal decrease. The only difference is the magnitude of the mean and the variance. For higher dynamic pressure, the mean and the variance are much higher than those of for lower dynamic pressure as indicated in figures 3.6 and 3.10.

The same general trend mentioned earlier is also observed for the probability density function for the porous wall tube as shown in figure 3.11. From the flow visualization, no slug formation is observed due to the pores of the wall. This is verified from the shape of the probability density function where all of the curves drop off gradually.

3.2.2 Average pressure

The average pressure was non-dimensionalized using the dynamic pressure and plotted against the standoff distance to nozzle diameter ratio for each tube diameter. The results are summarized in the log-log plots in figures 3.12 to 3.16. Most of the data falls onto a straight line. At high Z/d_o the curve levels off for the 38 mm and 51 mm solid tubes. From flow visualization, the distance where the graph starts to level off indicates the slug formation. The measured pressure is independent of the standoff distance once the slug forms. This is due to the fact that the distance where the slug forms stays at the same position and all of the jet energy is dissipating at that distance. Further increase in

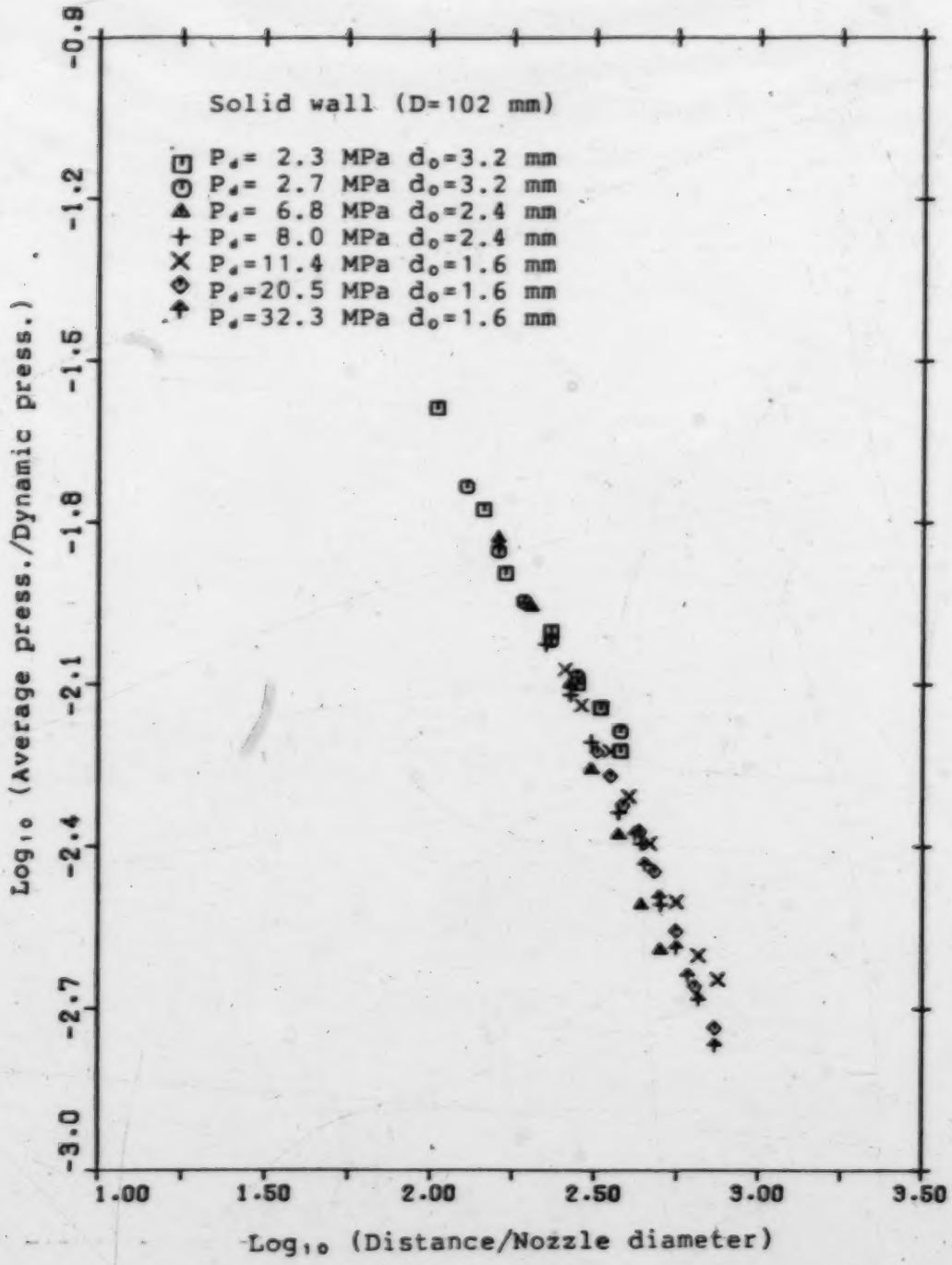

Figure 3.12 A plot of the non-dimensionalized average pressure against the non-dimensionalized standoff distance for the 102 mm diameter solid wall tube.

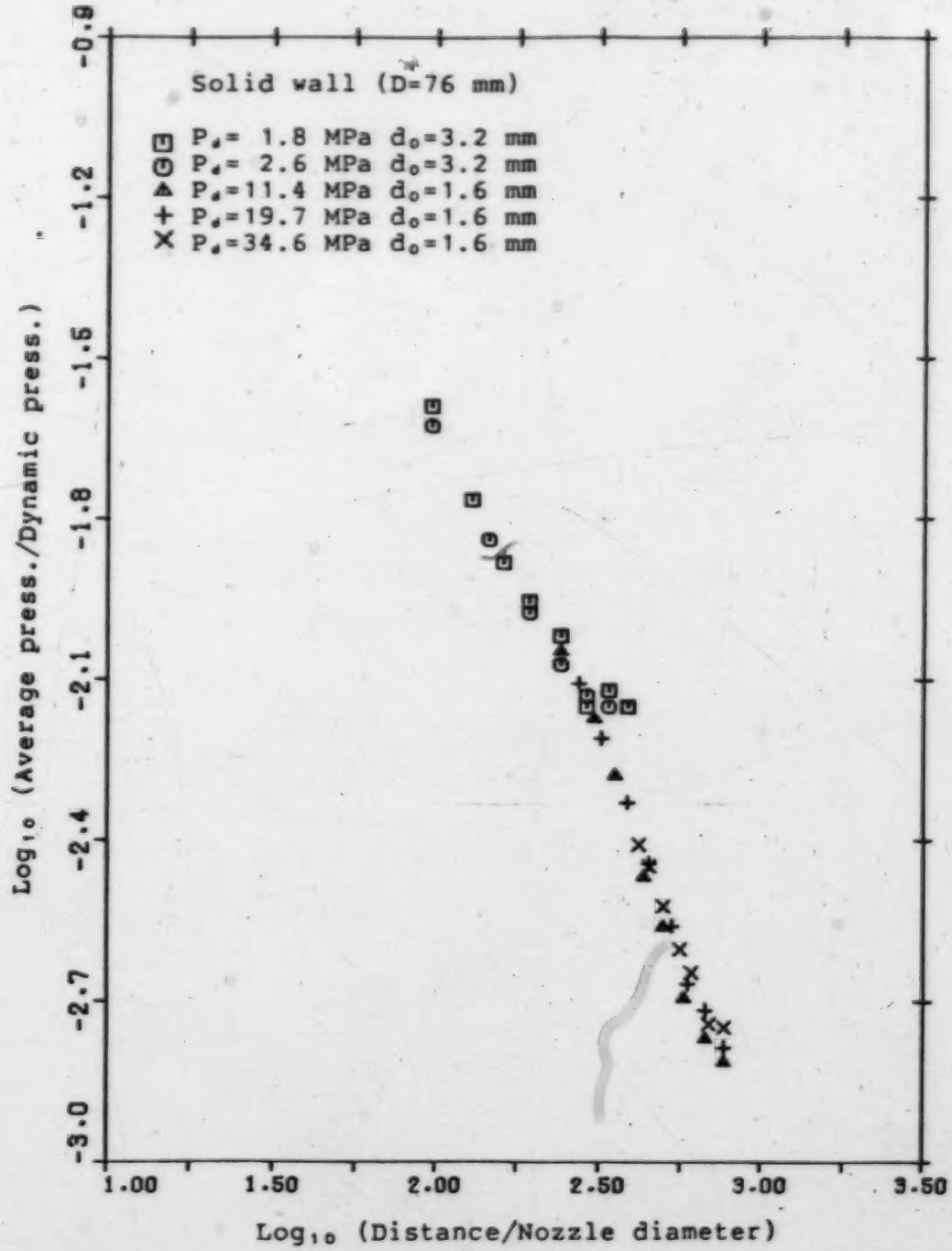

Figure 3.13 A plot of the non-dimensionalized average pressure against the non-dimensionalized standoff distance for the 76 mm diameter solid wall tube.

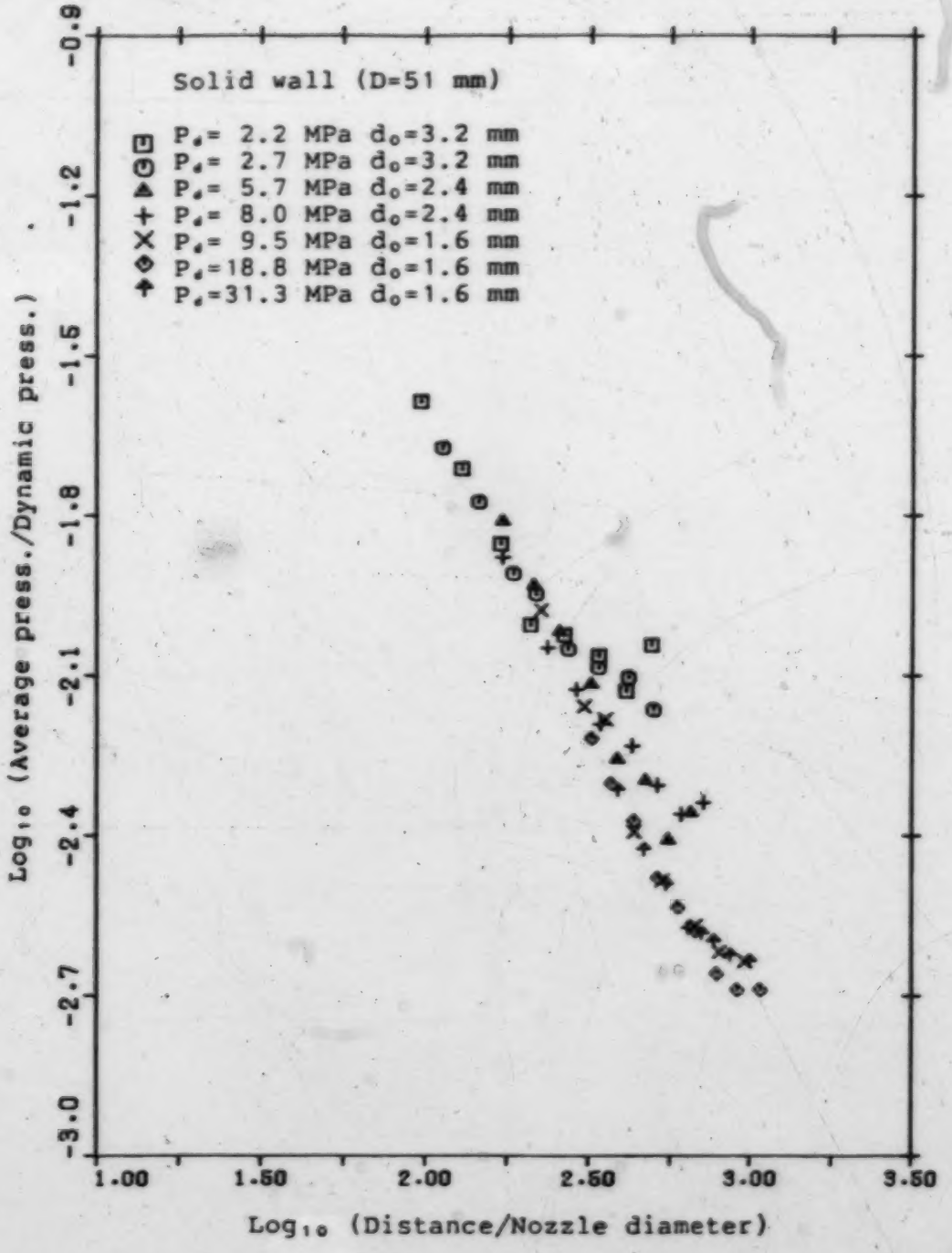

Figure 3.14 A plot of the non-dimensionalized average pressure against the non-dimensionalized standoff distance for the 51 mm diameter solid wall tube.

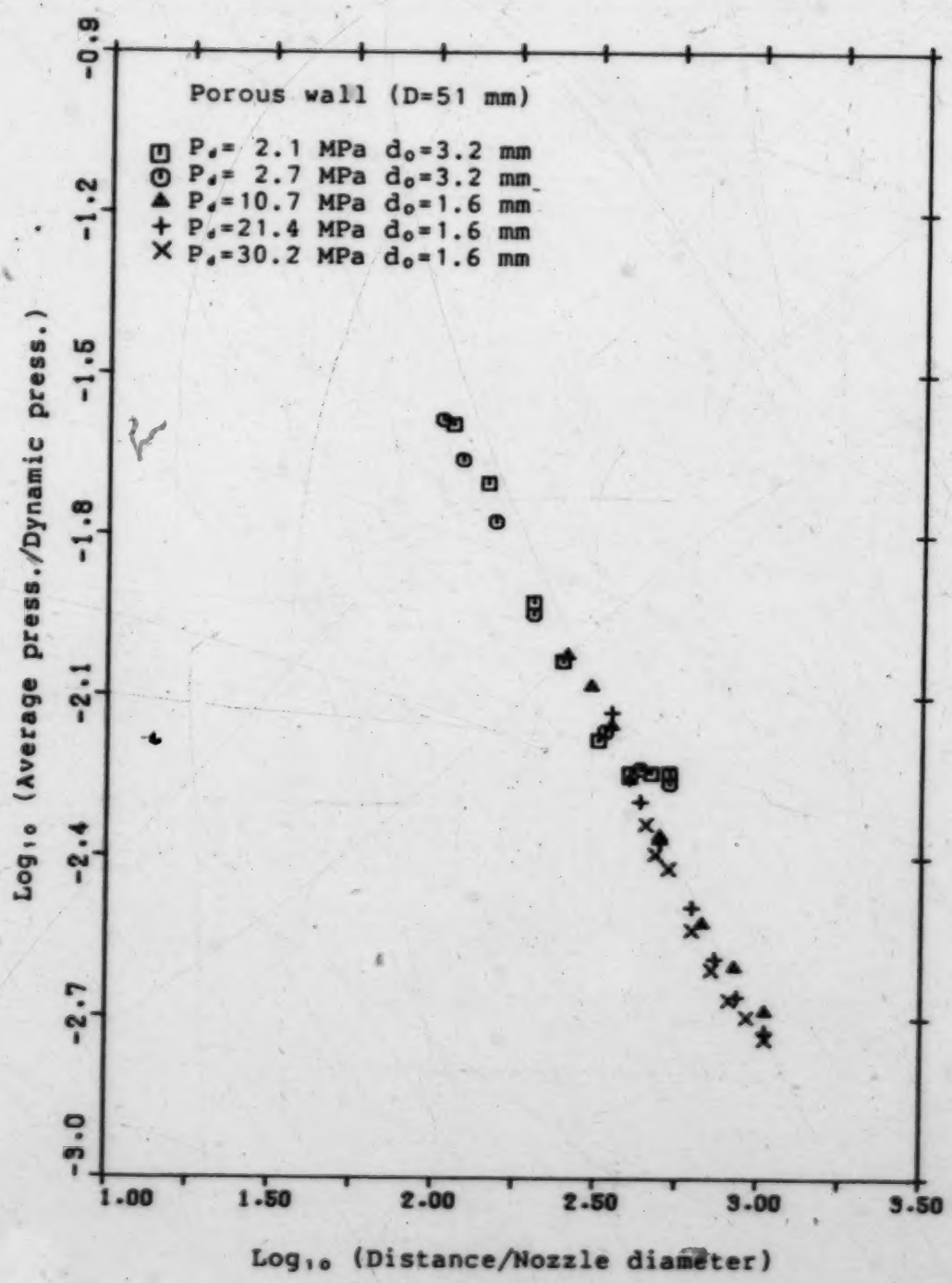

Figure 3.15 A plot of the non-dimensionalized average pressure against the non-dimensionalized standoff distance for the 51 mm diameter porous wall tube.

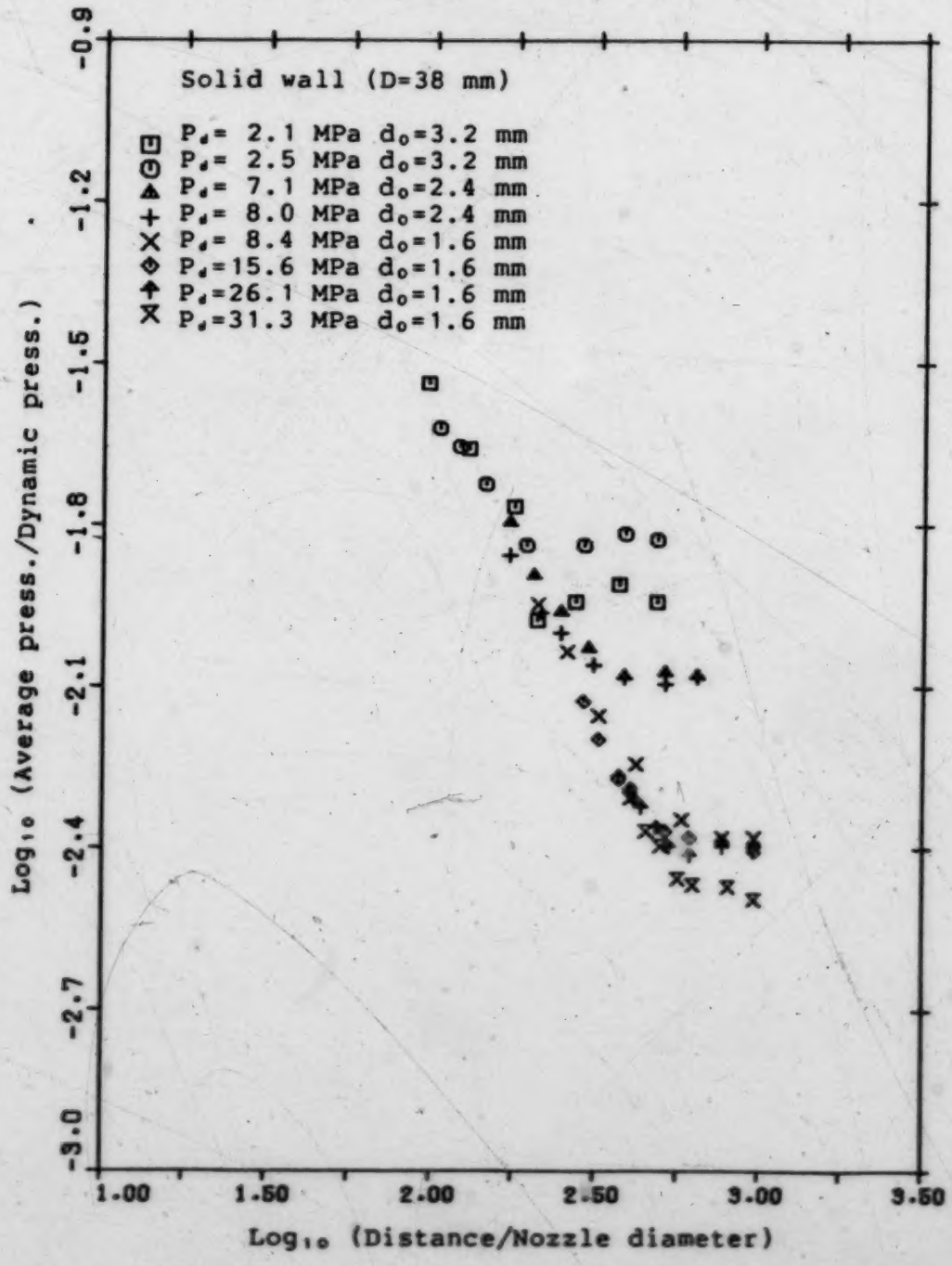

Figure 3.16 A plot of the non-dimensionalized average pressure against the non-dimensionalized standoff distance for the 38 mm diameter solid wall tube.

the standoff distance results in a lengthening of the slug with the upstream face remaining approximately in the same position. Also from these figures, it can be seen that the dependence of P ave/P_d with Z/d_o is independent of the tube size provided no slug forms. This is demonstrated by superimposing figures 3.12 to 3.16. All the data fall onto the same straight line and start to deviate only when the slug forms.

The results of the average pressure for the porous wall tests are plotted in figure 3.15. No slug formation was observed. This is confirmed from figure 3.15 where all the data falls onto a straight line, with no levelling off of the curve as in the solid wall cases.

4. Analysis of Results

Flow visualization observations and pressure signal records revealed that the effect of the water jet on the piston surface consists of a series of discrete impulses rather than a continuous but unsteady force associated with a coherent jet. It is suggested here then that an appropriate approach is to consider the jet impact to be a stochastic process and to develop a probabilistic model for predictions of ultimate depth of penetration and the cutting time required to reach that depth. In the model proposed here, it is first assumed that there is some critical pressure (Pc) that must be exceeded to cause failure at an oil sands surface. For each set of values of the standoff distance, nozzle diameter, nozzle pressure and tube diameter, the measured cumulative density function will then provide the probability that the critical pressure is exceeded, ie.

$$\mathcal{P}(p>Pc)$$

where $\mathcal{P}$: probability that the pressure exceeds Pc;

Pc: critical pressure;

p: pressure at the cutting face.

Holding all parameters constant except standoff distance, a plot of this probability against standoff distance can be made. Now if it is further assumed that $\mathcal{P}(p>Pc)$ must exceed some value $\mathcal{P}^*$ for a non-neglible cutting rate to occur, the

ultimate depth of penetration can be determined. In addition, if a relation between the penetration rate and the probability is known, an estimate of the time required to reach the maximum depth can be obtained. The details of this model will now be presented.

4.1 Prediction of Maximum Depth of Penetration

First, an estimate for a critical pressure is required. This estimate may be obtained by examining the experimental results of Chau (1980). Chau observed that no penetration of oil sands occurs at standoff distances greater than 200 mm when the dynamic pressure of water jet falls below 1.2 MPa from a 1.6 mm diameter nozzle. Although the dynamic pressure at the nozzle outlet is known, no information on the pressure at the cutting face was obtained by Chau. To obtain an estimate of this, the above conditions were duplicated including the use of the *same* nozzle. Plots of the probability and cumulative density functions were recorded and are shown in figure 4.1. Using the assumption that no significant cutting of oil sands occurs when the probability P that the pressure exceeds the critical value falls below 5%, a critical pressure of 70 kPa was determined (see figure 4.1).

With this value for a critical pressure, the probability that the pressure at the face of the piston is greater than Pc for various distances was obtained from the measured cumulative density functions. These probabilities

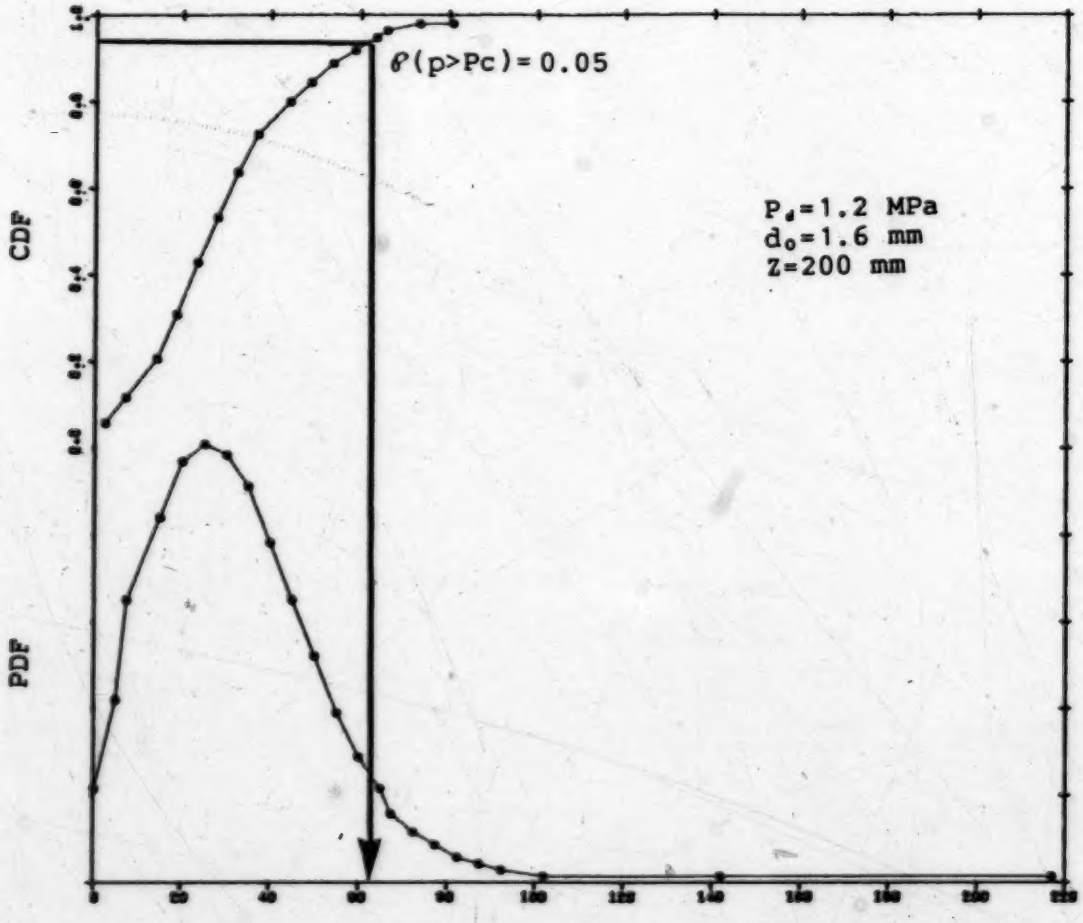

Figure 4.1 Probability and cumulative density function using the same nozzle as Chau (1980).

were obtained based on non-slug experimental data. It was assumed that the depth of penetration reached its maximum depth when the slug formed. These probabilities are provided in figures 4.2 to 4.6. To each set of data a curve of the form:

$$\mathcal{P} = \exp(-\lambda(Z/d_o)^2) \qquad (1)$$

was fitted where

Z : depth of penetration;

d_o : nozzle diameter;

and λ is a parameter that depends on the dynamic pressure P_d, nozzle diameter d_o, and tube diameter D.

The curve of this form was chosen because the rapidly decreasing probability with distance from the nozzle appears to be exponential in nature. The quadratic form of Z/d_o was chosen instead of the linea one because it would be expected that $\mathcal{P}(p>Pc)$ would be near one for some distance before beginning to decrease.

The values of λ in equation (1) for the various test conditions were determined by the method of least squares and the results are plotted in figure 4.7. From this figure, it can be seen that for the range of the current tests, λ depends most strongly upon the dynamic pressure at the nozzle. This parameter λ is observed to be approximately inversely proportional to dynamic pressure. A relationship

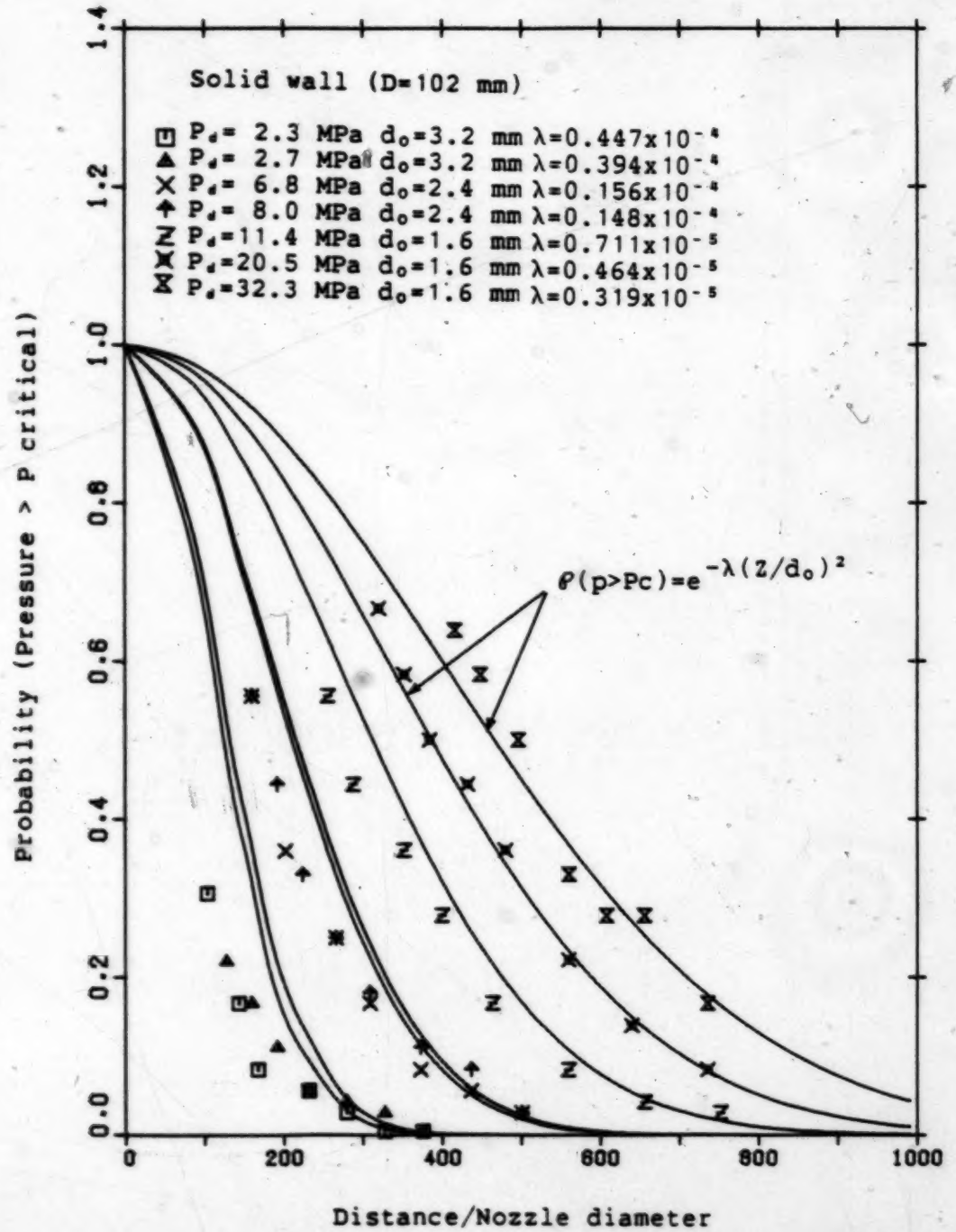

Figure 4.2 The probability that the pressure at the piston face exceeds the critical value for some combinations of nozzle diameter and pressure in the 102 mm diameter tube.

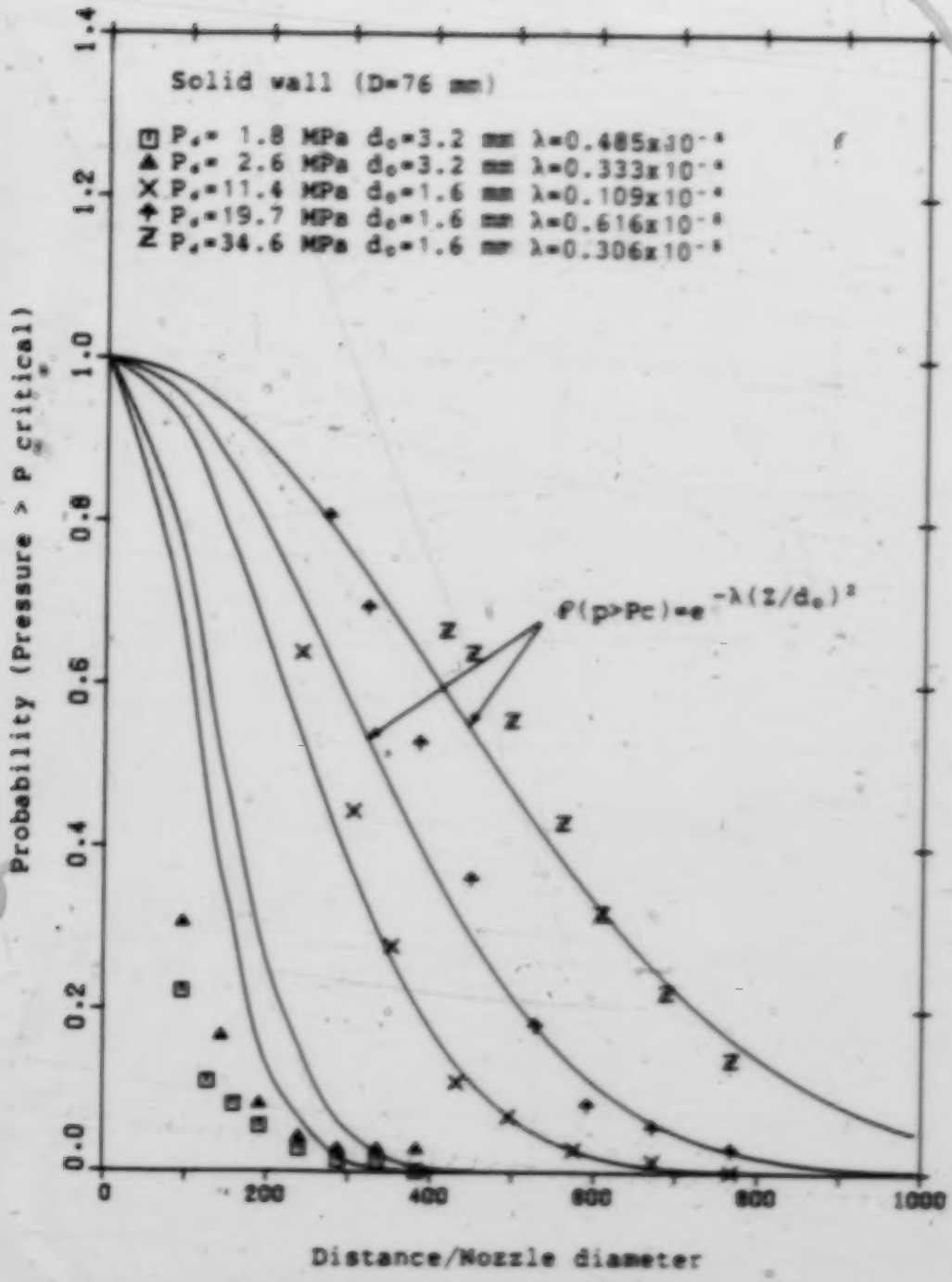

Figure 4.3 The probability that the pressure at the piston face exceeds the critical value for some combinations of nozzle diameter and pressure in the 76 mm diameter tube.

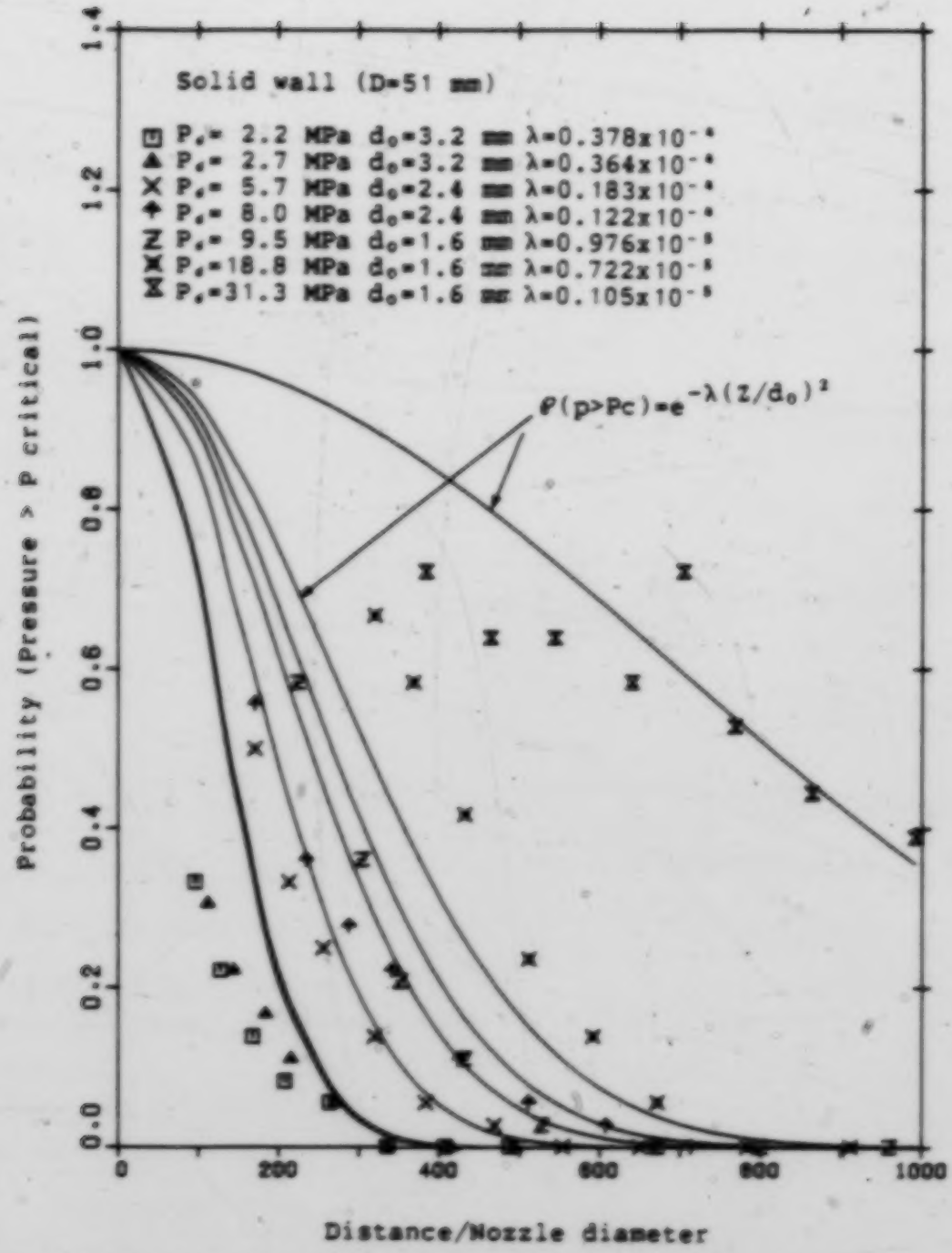

Figure 4.4 The probability that the pressure at the piston face exceeds the critical value for some combinations of nozzle diameter and pressure in the 51 mm diameter solid tube.

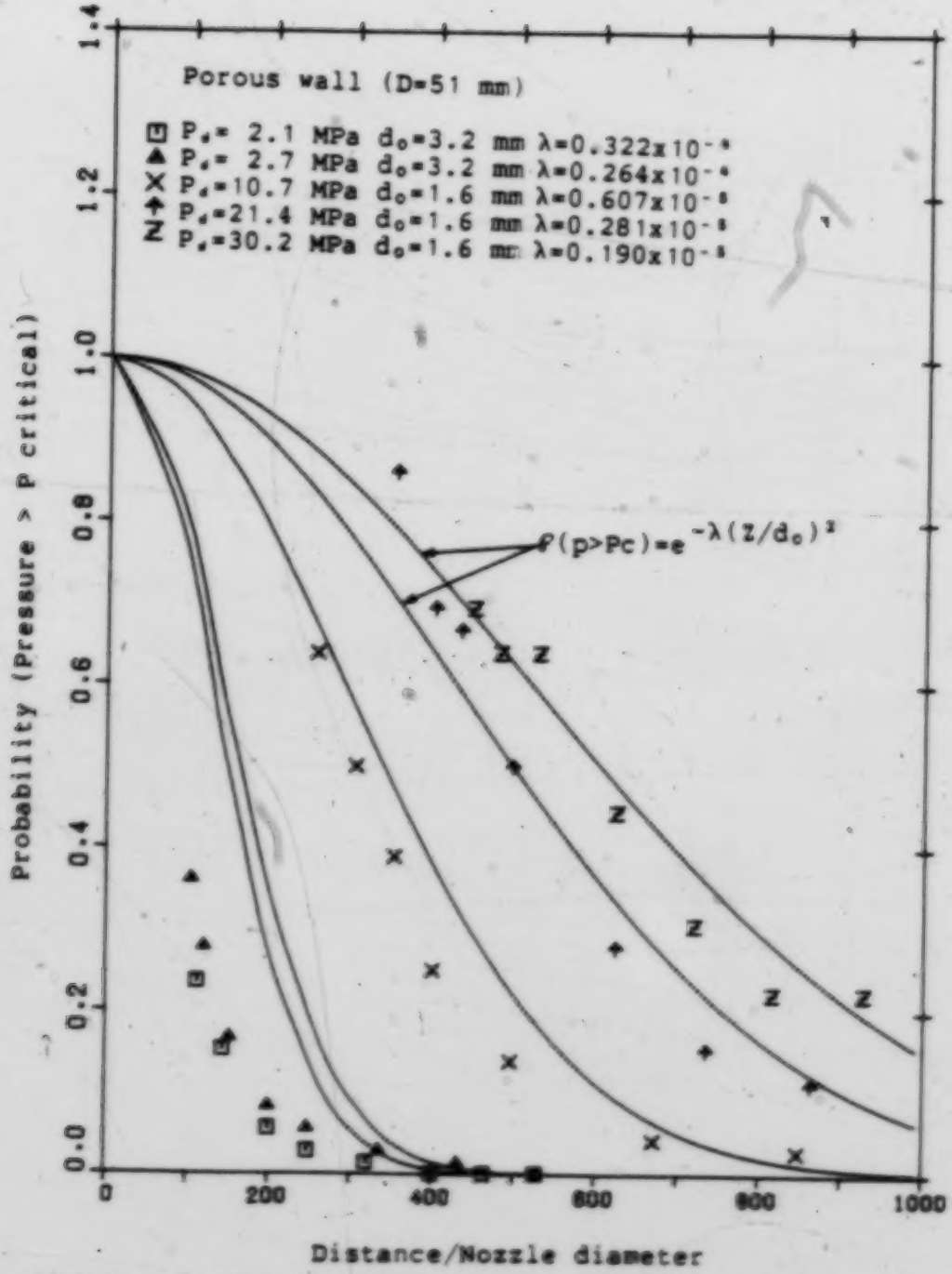

Figure 4.5 The probability that the pressure at the piston face exceeds the critical value for some combinations of nozzle diameter and pressure in the 51 mm diameter porous tube.

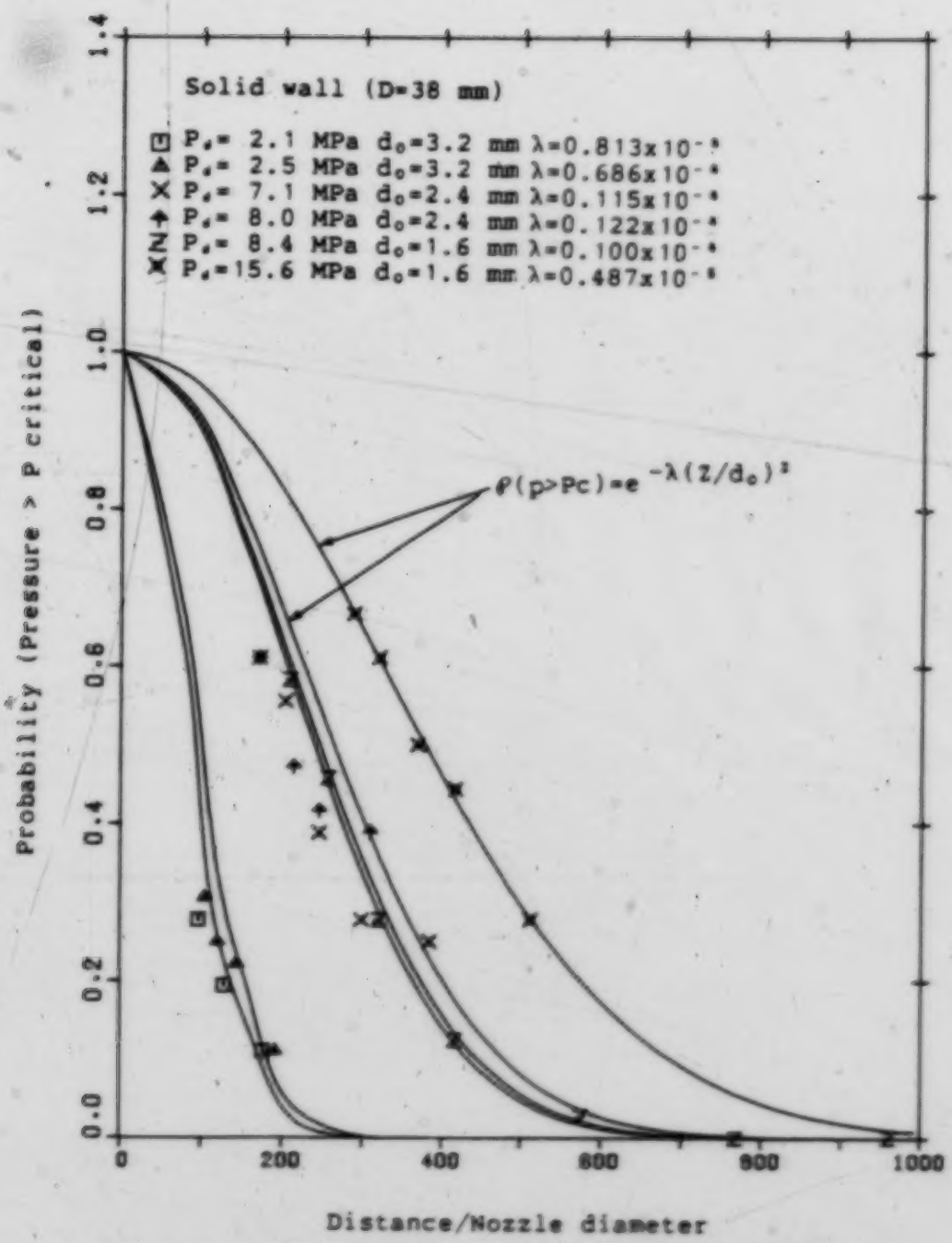

Figure 4.6 The probability that the pressure at the piston face exceeds the critical value for some combinations of nozzle diameter and pressure in the 38 mm diameter tube.

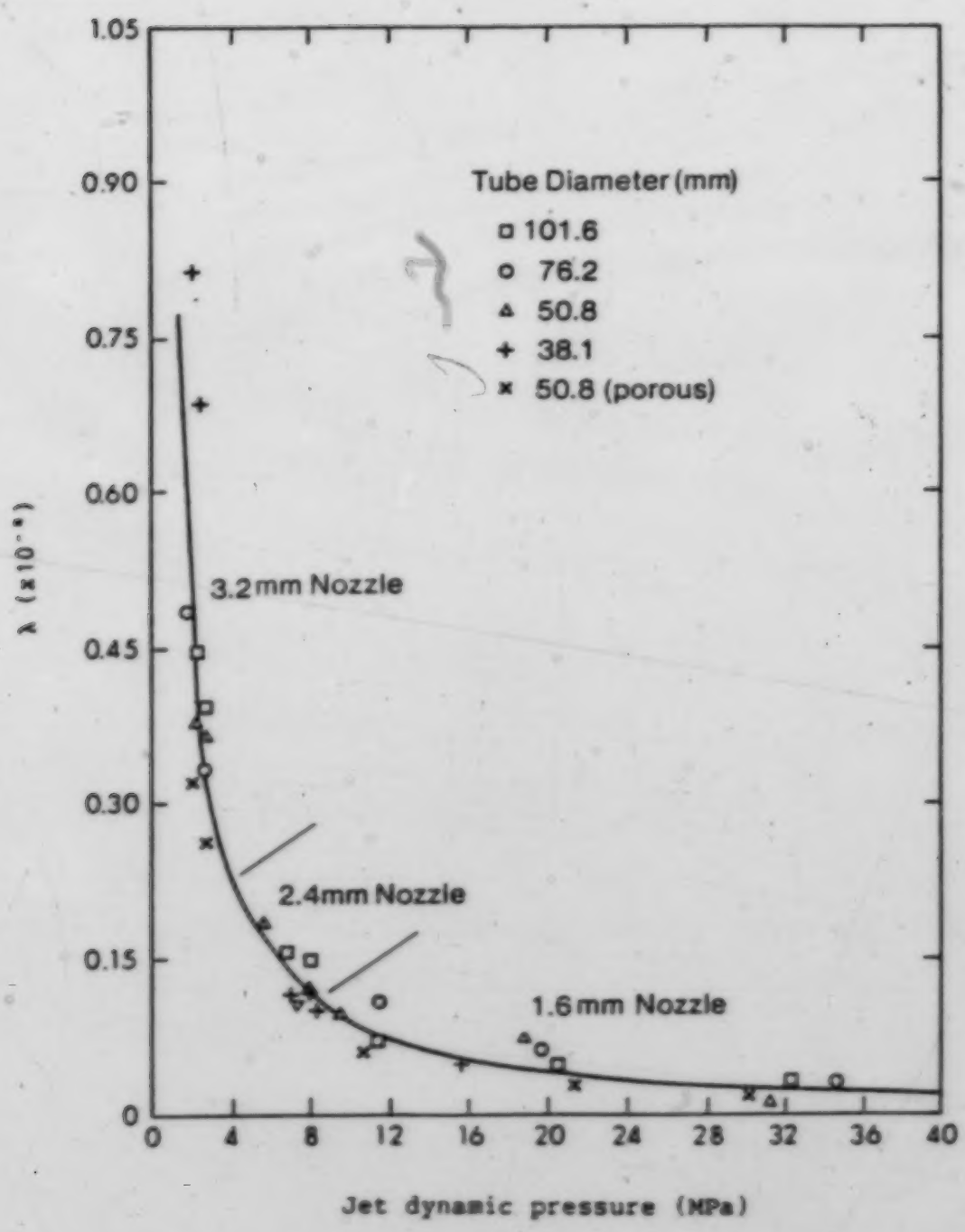

Figure 4.7 The variation of the parameter λ with dynamic pressures for different tube and nozzle diameters.

between λ and dynamic pressure was assumed as follows:

$$\lambda = a/P_d^k \qquad (2)$$

where a and k were determined by least squares method to be:

$a = 0.1119 \times 10^{-3}$

$k = 1.0986$ where P_d is given in MPa.

Therefore, equation (1) can be rewritten as:

$$P = e^{-\left\{\frac{a}{P_d^k}\right\}\left\{\frac{z}{d_o}\right\}^2} \qquad (3)$$

It is further assumed that no cutting occurs when the probability that the pressure exceeds critical pressure falls below 5%. Substituting a probability of 5% into equation (3), the resulting prediction of maximum depth of penetration becomes:

$$Zult = \sqrt{(-(d_o^2 P_d^k \ln c)/a)} \qquad (4)$$

where $c = 0.05$

This equation can be simplified approximately to:

$$Zult \cong 165\, d_o \sqrt{P_d} \qquad (5)$$

where Zult is in mm;

d_o is in mm;

P_d is in MPa.

The dynamic pressure of the water jet is related to the volume flow rate by:

$$P_d = \frac{1}{2}\rho\left\{\frac{4Q}{\pi d_o^2}\right\}^2 \times 10^{-6} \quad (\text{MPa}) \qquad (6)$$

where ρ : density of water;

Q : volume flow rate of water jet.

Therefore, equation (5) can be also approximated by:

$$Zult \cong 4.7 \times 10^{-3} \frac{Q}{d_o} \qquad (7)$$

where Q is in m^3/sec;

d_o is in mm;

Zult is in meter.

The above relation shows the dependence of the ultimate depth to the flow rate and nozzle diameter, and is valid for conditions where no slug forms.

4.2 Prediction of Cutting Time

The time to reach the ultimate depth is another parameter of interest for an operator of this water jet instrument. It is required to predict the water requirements

for this type of application.

Numerous cutting relations might be proposed, however, one assumption is of direct proportionality between the rate of cutting and the probability that the critical pressure is exceeded. A better cutting relationship could be investigated; however, before any more complex treatment of this model is carried out, a simple model approach will be done. Hence the rate of penetration based on the direct proportionality takes the form:

$$dZ/dt = B\rho \qquad (8)$$

where dZ/dt : cutting rate, and

B : a parameter which has dimensions of length per unit time.

This parameter B can be interpreted as the initial cutting rate, because at time t=0, the probability of the pressure exceeding critical pressure Pc (provided P_e>Pc) is equal to one. Substituting equation (3) into equation (8), and integrating yields

$$t = \frac{1}{B}\int_0^Z e^{\left\{\frac{a}{P_d^k}\right\}\left\{\frac{z}{d_o}\right\}^2} dz \qquad (9)$$

which gives the time necessary to reach a given depth of cut Z. In particular, with the ultimate depth given by equation

(4), the time required is:

$$tult = \frac{1}{B} \int_{0}^{Z_{ult}} e^{\left\{ \frac{a}{P_d^k} \right\} \left\{ \frac{z}{d_o} \right\}^2} dz \qquad (10)$$

The value of the parameter B was determined from the laboratory data of Chau (1980). Only the data obtained from 1.6 mm nozzle diameter could be used, because the dynamic pressures for other nozzle diameters were rather low. The value of B in general would be a function of standoff distance, dynamic pressure, nozzle diameter, and material properties. The method to obtain this parameter B is illustrated in the appendix B. The resulting initial cutting rates for different dynamic pressures are plotted in figure 4.8.

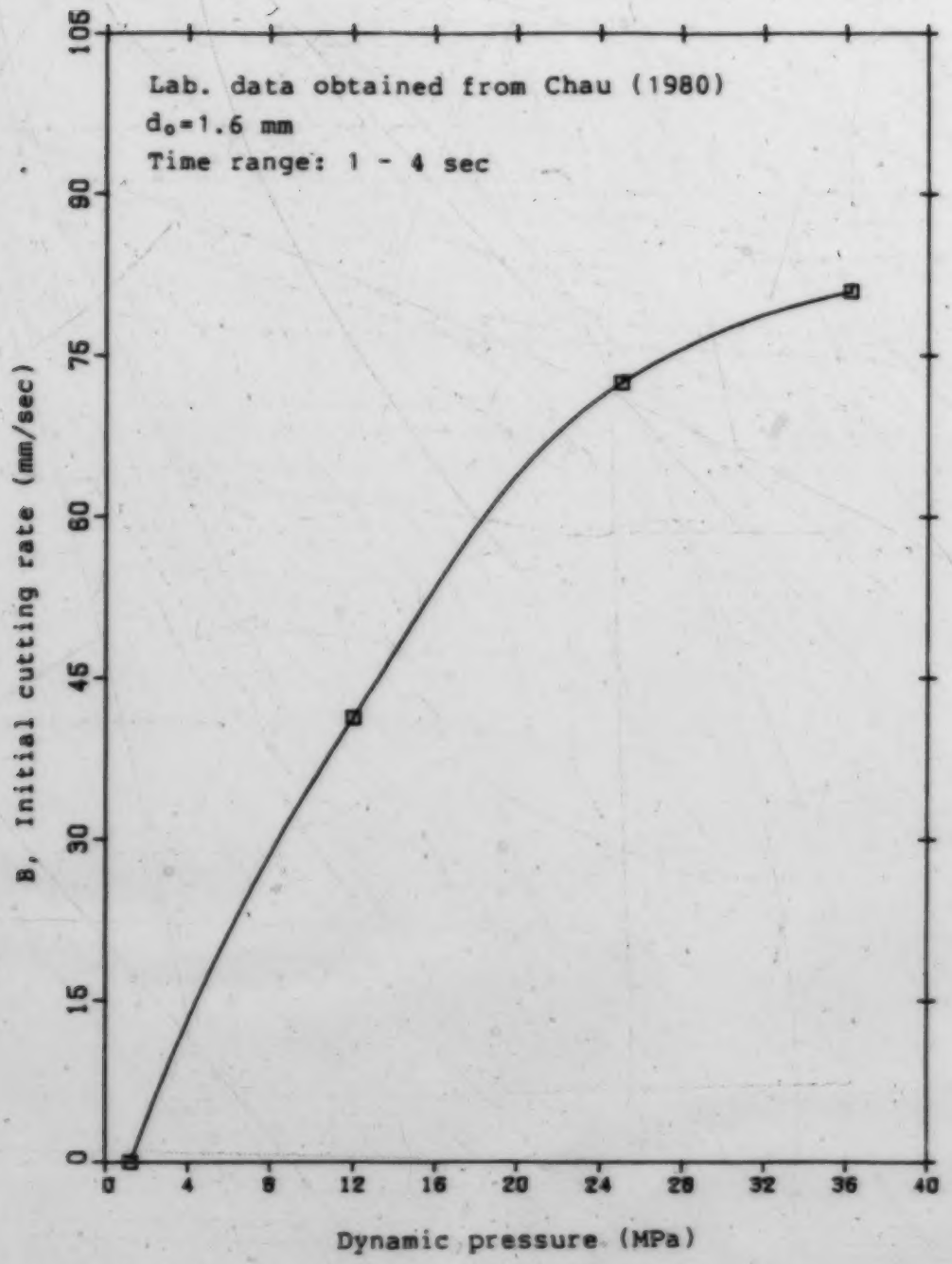

Figure 4.8 Estimates of the parameter B based upon best fits of equation (9) to the laboratory data of Chau (1980).

5. Discussion of Results

5.1 Comparisons of prediction and other correlations

The depth of penetrations predicted using equation (9) for 3 different dynamic pressures are plotted and compared with some field test data (Gilpin, 1981) in figure 5.1. As can be seen from this figure, the prediction of the depth of penetration agrees fairly well with the field results. A maximum of 8% deviation for the dynamic pressure of 17 MPa was observed between the prediction and the field test results. For the 12 MPa case the comparison is not so promising. However the large scatter in the field data makes a meaningful comparison difficult. The scatter in the field test results is believed to be due to the orientation of the bedding planes. This orientation is not taken into consideration in the laboratory correlation developed here.

A comparison between field test results and predicted ultimate depth of penetration for various dynamic pressures is shown in figure 5.2. Most of the field test data are below the predicted ultimate depth which is as expected, for the ultimate depths were not attained. All of the data available from the field tests is for very short jetting times (60 seconds). The cutting times predicted for the ultimate depth are much longer(eg. 300 sec vs 60 sec). Hence, no conclusive comparison can be made on the predicted ultimate depth or required cutting time.

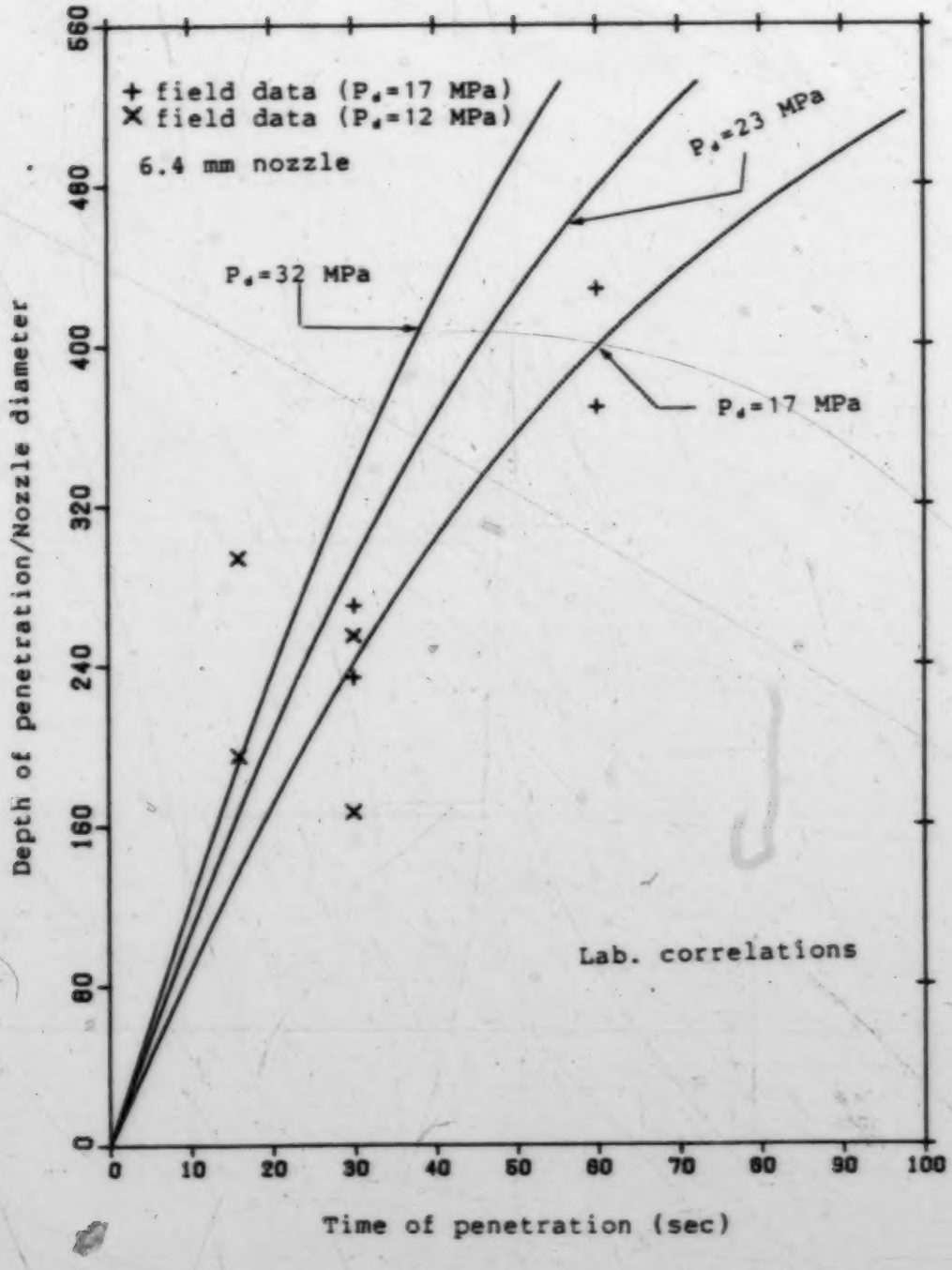

Figure 5.1 A comparison between depths of penetration predicted by equation (9) and the field data of Chau (1980) for a 6.4 mm diameter nozzle.

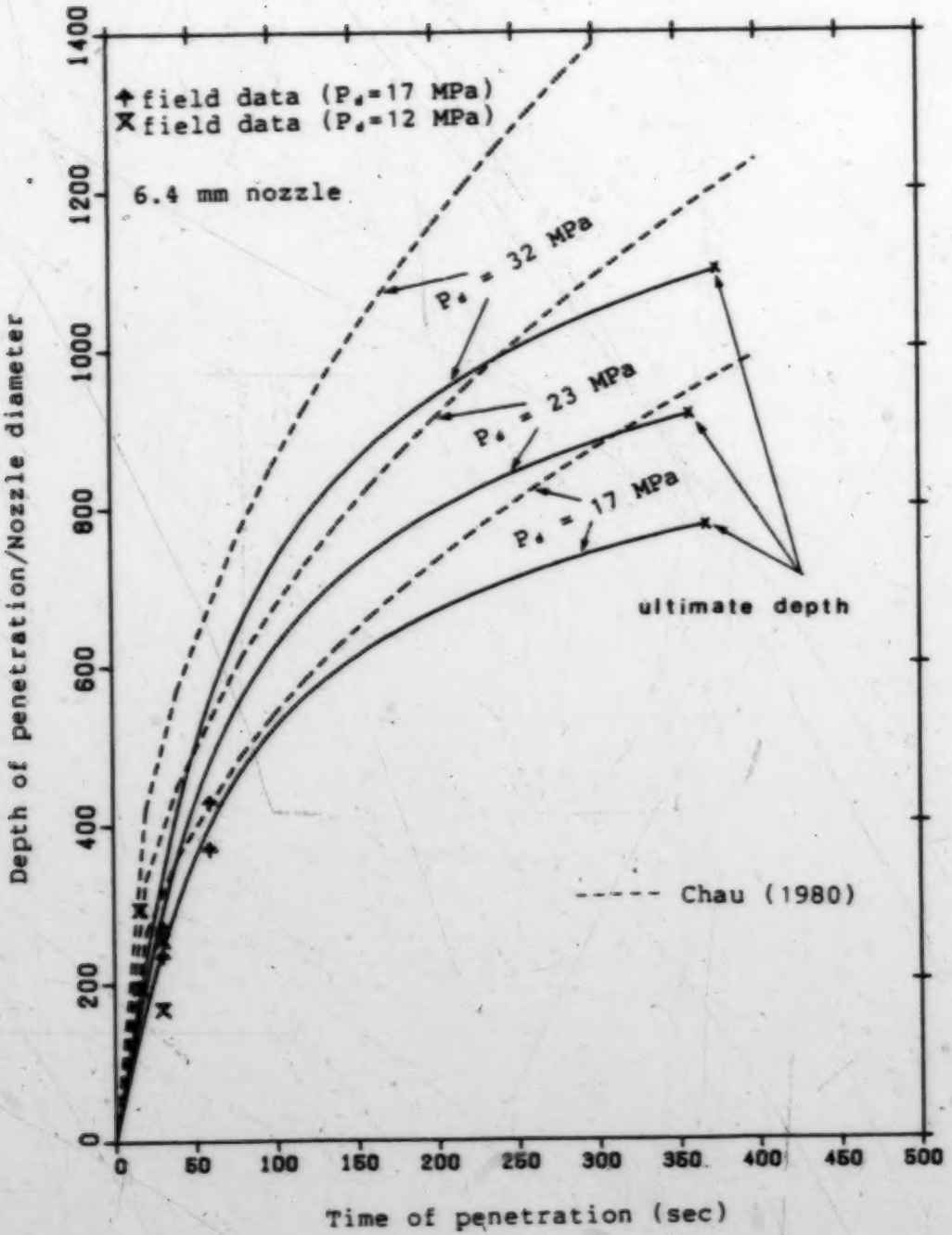

Figure 5.2 An estimate of the time required to reach the predicted ultimate depth of penetration

Also plotted in figure 5.2 are the predicted depths of penetration for a continuous jet using the correlation developed for recompacted oil sands (Chau, 1980). The results show that the depth of penetration based on the probabilistic model is lower than that of the correlation developed by Chau. This is not too surprising as first Chau's correlation is based on laboratory data for very limited jetting times (4 seconds). Second, Chau's correlation predicts no limiting depth but states the depth should continue to increase indefinitely in proportion to the 0.44 power of time.

The ultimate depth of penetration predicted by Gates et al. (1982) is compared with the present correlation for various dynamic pressures in figure 5.3. This plot shows that the ultimate depth predicted based on a confined jet is slightly below that of unconfined jet for dynamic pressure below 24 MPa. As the dynamic pressure increases, the predicted depth based on confined jet is higher than that of unconfined jet.

The simplified form of the ultimate depth given by equation (5) shows the ultimate depth is proportional to the nozzle diameter and square root of the dynamic pressure. Thus increasing the nozzle diameter or dynamic pressure will cause the maximum depth of penetration to increase as well. Increasing the volume flow rate will also increase the ultimate depth of penetration as seen from equation (7).

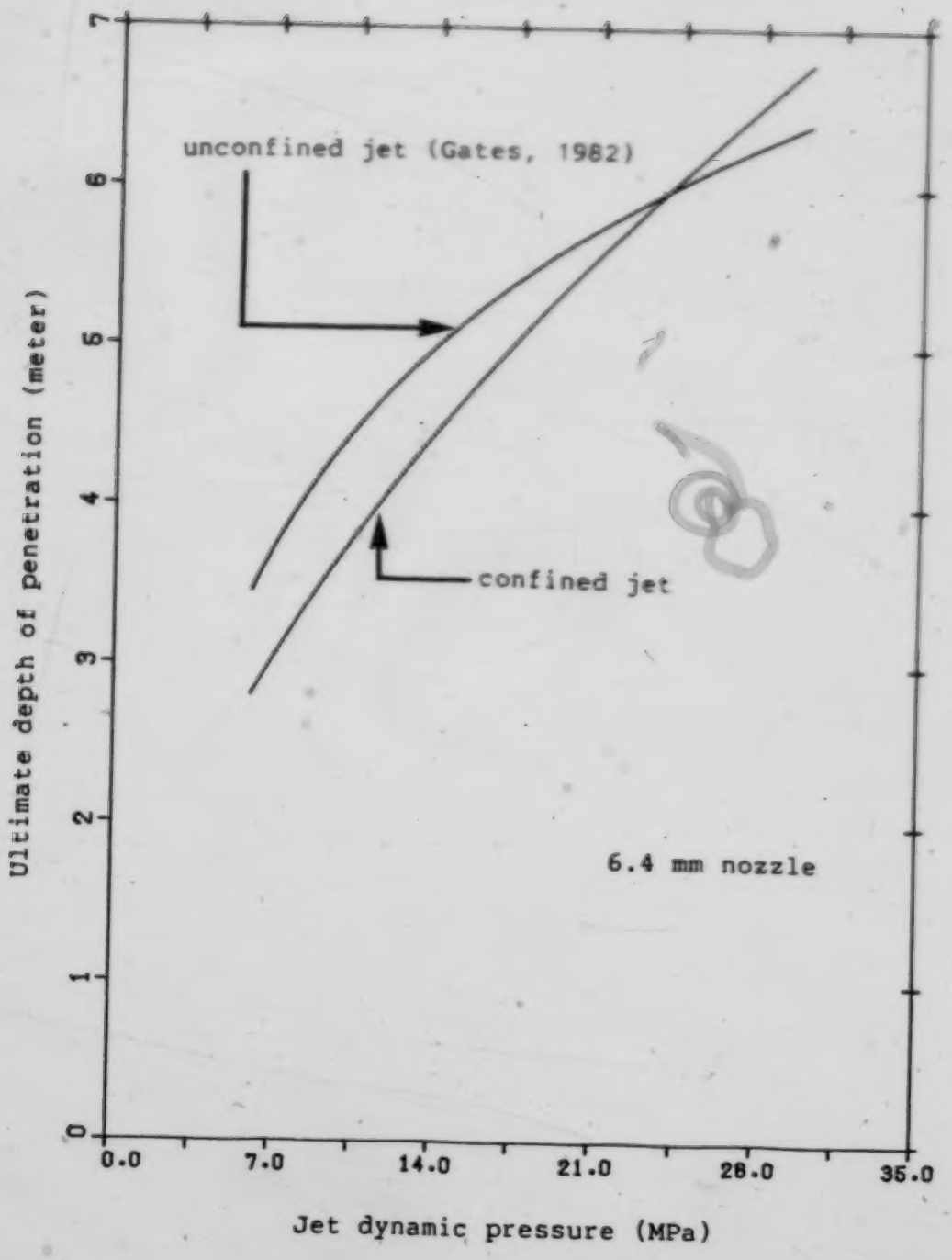

Figure 5.3 A comparison of ultimate depths predicted by the present correlation with that predicted by Gates et al. (1982).

5.2 Influence of some assumptions in the empirical model

It has been assumed that when the probability that the pressure exceeds a certain critical pressure falls below a given value, an ultimate depth has been reached. Hence, this approach depends on the critical probability chosen. Figure 5.4 shows the dependence of critical pressure obtained on the probability chosen. If the probability that the pressure exceeds the critical pressure increases, the corresponding critical pressure decreases and vice versa. For example, if a critical probability of 30% was chosen, the corresponding critical pressure that must be exceeded is found to be 40 kPa as shown in figure 5.4. Based on this critical pressure, new experimental constants for equation (3) can be obtained. The ultimate depth of penetration predicted using a critical probability of 30% was about 25% higher than the one predicted using a critical probability of 5%. The critical pressure depends on the material properties and other factors such as the overburden pressure and the orientation of the bedding planes in the formations. More data would be very beneficial in providing a better estimate of this quantity.

The simple linear relationship assumed here for the penetration rate seems to provide a reasonable estimate of the time of penetration. Physically, however it is unsatisfying since it means that the rate of penetration is independent of the pressure at the cutting face. A more reasonable relationship for the cutting rate can be proposed

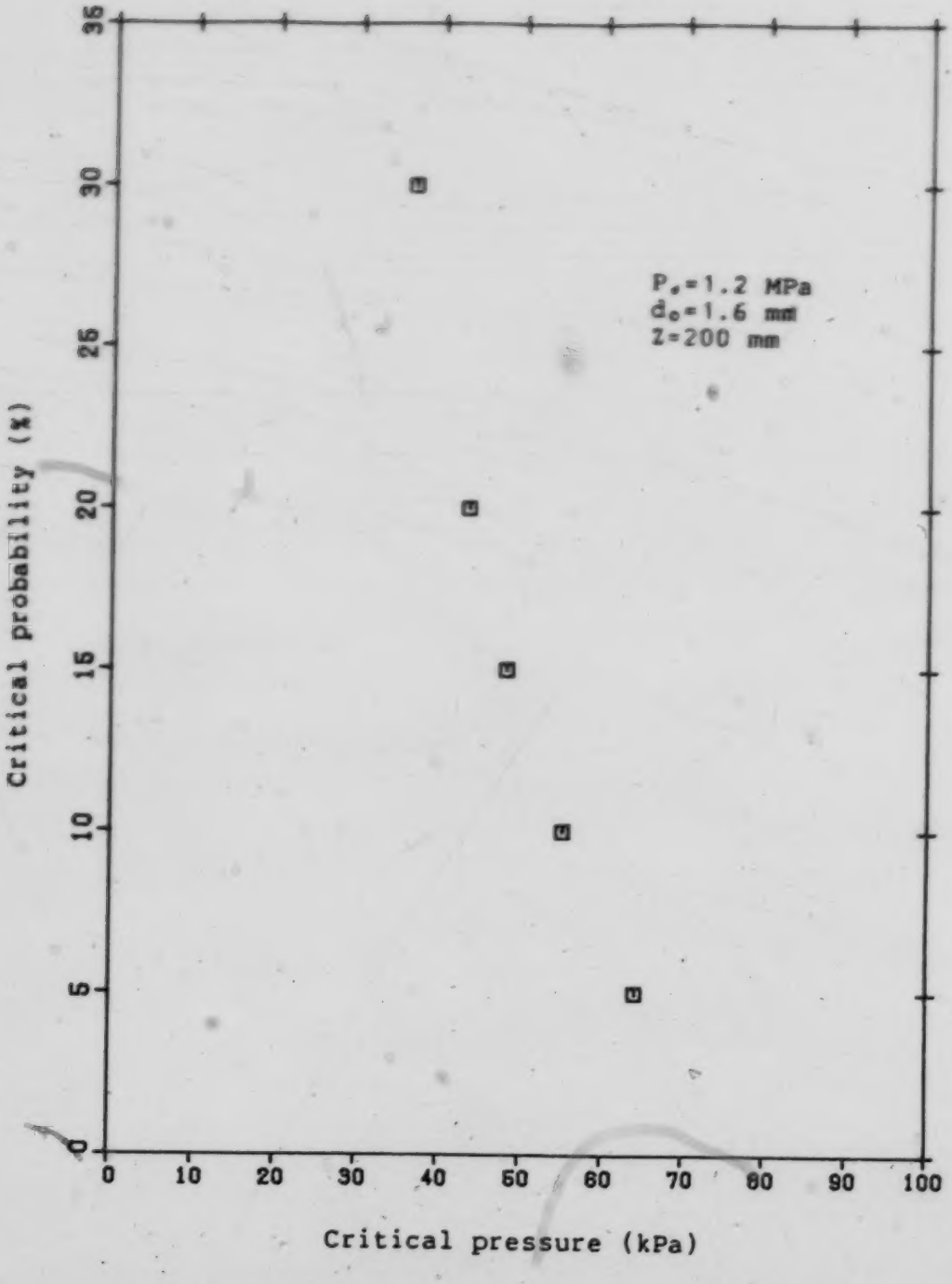

Figure 5.4 The dependence of critical pressure on the critical probability chosen.

by including the effect of the amount by which the expected value of pressure exceeds the critical cutting pressure.

The correlation developed was based on the non-slug experimental data. When the slug forms as in the case of 38 mm and 51 mm tube diameters, the depth is assumed to have reached its ultimate value. From figure 3.12 to 3.16, it can be seen that as long as no slug forms, all of the average pressure data from different tube diameters fall onto the same curve. The point where the graph deviates from this line indicates the beginning of the slug formation. This is verified from the flow visualization results. Hence the absence of the influence of tube diameters can be seen on the correlation equation developed.

The present laboratory data was obtained using relatively small nozzle diameters. It might be expected that the characteristics of the small jets are different from those of a much larger jet (Davies et al., 1980). Therefore, any extrapolation to a larger diameter jet for the correlation developed must be done in a cautious manner.

Besides the basic nozzle design itself, the effect of the nozzle geometry was not investigated in the present work primarily because of a 90 degree elbow immediately upstream of the nozzle. This sharp turn creates secondary flow which reduces the coherence of the jet and is likely to nullify any gain in jet coherence due to careful nozzle design.

5.3 Differences between the simulated and actual down-hole geometry

Many factors have not been incorporated into the present experimental model of the down-hole geometry. These include for example, orientation of the bedding planes, overburden pressure, porosity and permeability. Due to the inhomogeniety of the oil sands, complete modelling in the laboratory model would not in any event be possible.

The formation of a slug of water in different tubes as in the case of 38 mm and 51 mm tube diameters depends on the volume flow rate and the standoff distance. Whether the slug will form in the real case can not be determined at this stage due to the unknown effects of the porosity and permeability of the oil sands. Only a very preliminary set of experiments on the effect of the porosity was performed. The permeability of this set-up was very low due to large hole size. Questions as to the size of holes and methods of obtaining representative values for porosity and permeability are by themselves of interest.

5.4 Consequences of the predictions

For a nozzle diameter of 6.4 mm and dynamic pressure of 23 MPa, the ultimate depth of penetration is predicted to be 5.9 meters and is achieved with a jetting time of 6 minutes. This result is very encouraging and shows the capability of using water jets to punch out holes in the oil sands formation. In addition to depths of penetration another

quantity of interest is the water requirements.

A plot of the water requirements versus dynamic pressure of the water jet to reach the ultimate depth of penetration can be seen in figure 5.5. The plot shows that as the dynamic pressure increases, more water is required to reach the ultimate depth of penetration. No optimum value for the water requirements is observed from this plot. It can be seen from this figure that there is no particular advantage in going to a much higher jet dynamic pressure for the water requirements will become excessive. For a dynamic pressure of 20 MPa, the ultimate depth of 5.4 meters is predicted with a jetting time of approximately 6 minutes. The water required to reach such depth is predicted to be 2.3 m^3. For a large number of holes to be drilled by this water jet, the water requirements will certainly increase. Removal of this spent water will have to be considered in any future implementation of this type of project (eg. gas lift). A pulsed jet might be of great interest in reducing the water requirements. Chau (1980) found that a pulsed jet always give a higher penetrating power than a continuous jet and this is a very promising result.

The model can not be conclusively evaluated because of the very limited field data available. No existing data on the ultimate depth of penetration on the actual tests can be found in any of the literature cited. To improve the evaluation of this model, a more complete set of field test data is needed.

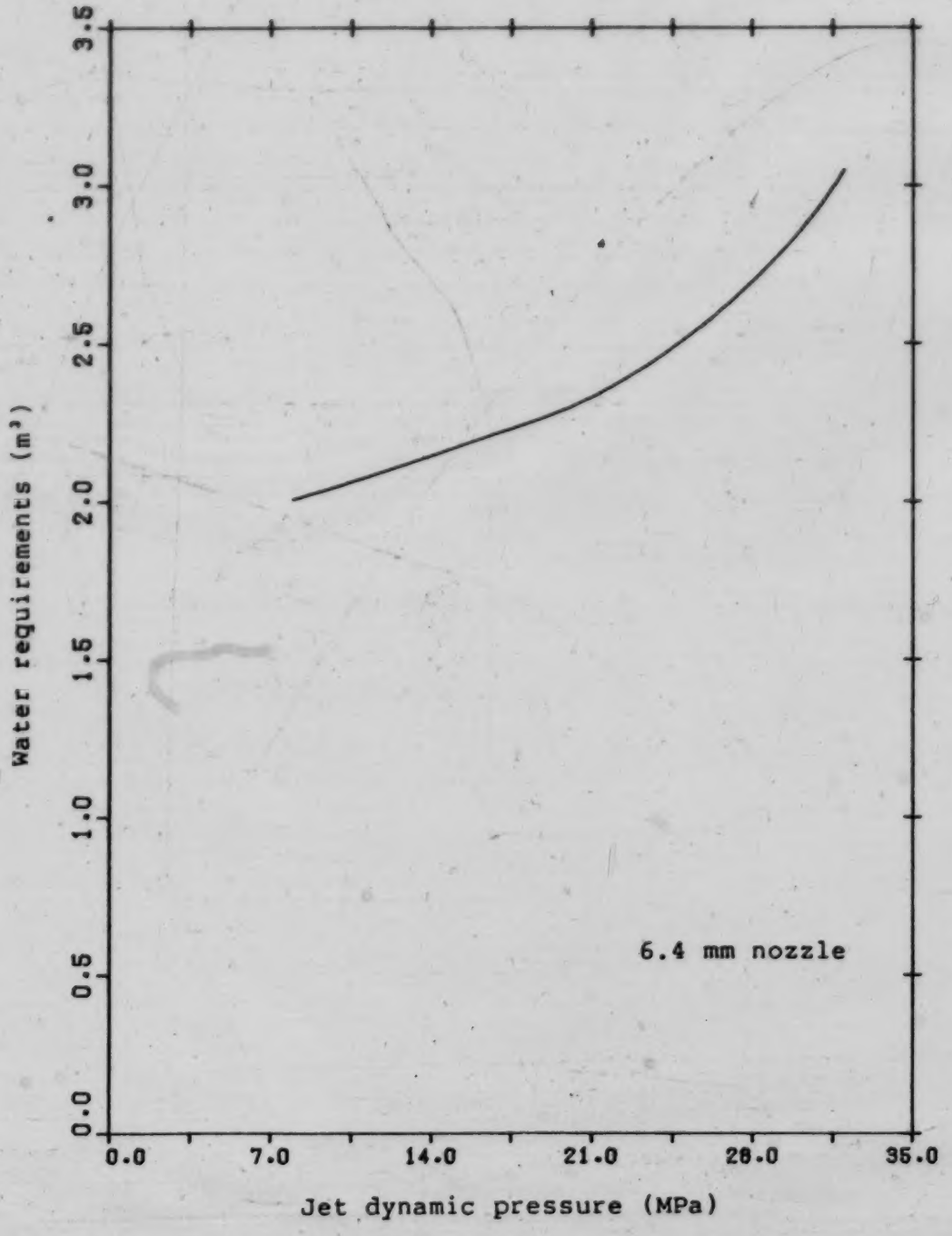

Figure 5.5 An estimate of the water requirements to reach the ultimate depth of penetration for various dynamic pressures.

5.5 Alternative model in jet cutting

The 'apparent' lack of fit for the low pressure results shown in figures 4.2 to 4.6 is due to the fact that the probability curves are being forced through one at Z/d_o equals zero. A better fit can be obtained by using a curve of the form:

$$P(p>Pc) = C\, e^{-\lambda_1 (Z/d_o)^2}$$

As can be seen, for example, in figure 5.6, at low pressures the probability of exceeding Pc is less than one. However, at some of the higher pressures this best fit gives values of the probability greater than one which is impossible. So then for the cases where C would exceed one, they are forced through one and hence the correlation is the same as the original one for these cases. The values of λ do not differ much between the first and second models as shown in figure 5.7. The influence of this second curve fit on the maximum depth of penetration is now depending on the values of the constant C and the probability assumed P as shown below:

$$Z_{max}/d_o = \sqrt{\frac{\ln\left\{\frac{C}{P}\right\}}{\lambda_1}}$$

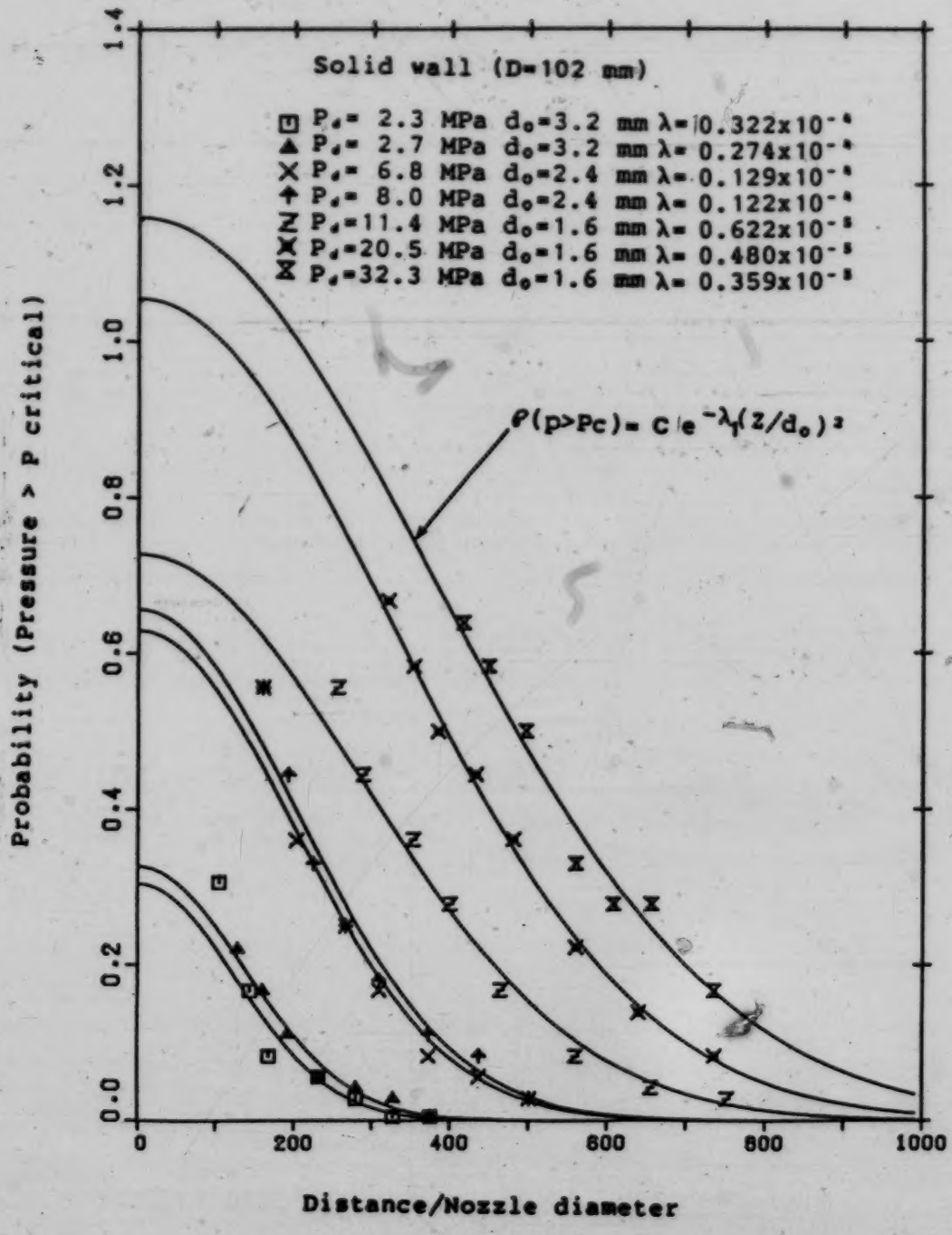

Figure 5.6 The probability that the pressure at the piston face exceeds the critical value for alternative model.

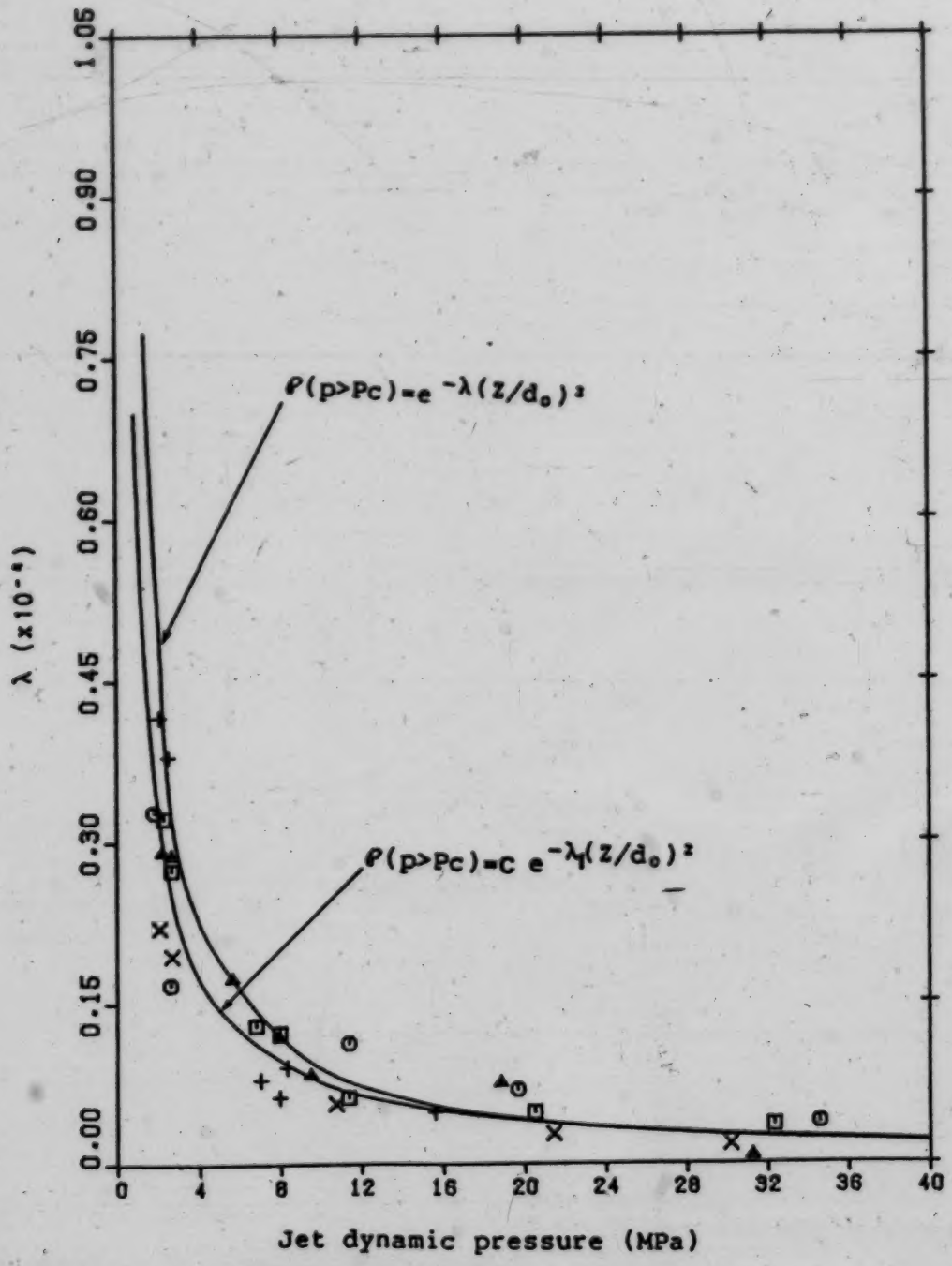

Figure 5.7 The variation of the parameter λ between the first and second model.

For the case of a low pressure jet (2 MPa, d_o=3.2mm):

Based on the first model: Zmax=765 mm

Based on the second model : Zmax=739 mm (C=0.3)

For the case of a high pressure jet (32 MPa):

Based on the first model : Zmax=3514 mm

Based on the second model : Zmax=3501 mm

However the influence upon the cutting rate is more significant particularly for the low pressure jets. If now the second curve fit to the probability is used, the cutting time becomes:

$$t = \frac{1}{BC} \int_{o}^{z} e^{\lambda_1 \left\{ \frac{z}{d_o} \right\}^2} dz$$

It can be seen that the cutting times for the low pressure jets become substantially longer. For example, for a 2 MPa jet, C=0.3, so the predicted cutting time would be 1.8 times longer than predicted by the first model. However for higher pressure cases the value of C is close to 1, e.g. for a 32 MPa jet, C=1.16 and the change in cutting time is 14%. A summary of various different parameters for the first and second models can be seen in table 5.1.

Table 5.1 Variation of the parameters between the first and second model.

P_a MPa	d_o mm	D mm	λ $\times 10^{-4}$	λ_1 $\times 10^{-4}$	C
2.3	3.2	102	0.447	0.322	0.30
2.7	3.2	102	0.394	0.274	0.33
6.8	2.4	102	0.156	0.129	0.63
8.0	2.4	102	0.148	0.122	0.66
11.4	1.6	102	0.071	0.062	0.73
20.5	1.6	102	0.046	0.048	1.06
32.3	1.6	102	0.032	0.036	1.16
1.8	3.2	76	0.485	0.328	0.22
2.6	3.2	76	0.333	0.167	0.19
11.4	1.6	76	0.109	0.113	1.18
19.7	1.6	76	0.062	0.069	1.33
34.6	1.6	76	0.031	0.039	1.38
2.2	3.2	51s	0.378	0.290	0.26
2.7	3.2	51s	0.364	0.287	0.30
5.7	2.4	51s	0.183	0.173	0.75
8.0	2.4	51s	0.122	0.117	0.87
9.5	1.6	51s	0.098	0.083	0.42
18.8	1.6	51s	0.072	0.075	1.23
31.3	1.6	51s	0.011	0.007	0.81
2.1	3.2	51p	0.322	0.221	0.15
2.7	3.2	51p	0.264	0.195	0.29
10.7	1.6	51p	0.061	0.057	0.76
21.4	1.6	51p	0.028	0.028	1.00
30.2	1.6	51p	0.019	0.018	0.92
2.1	3.2	38	0.813	0.416	0.40
2.5	3.2	38	0.686	0.379	0.46
7.1	2.4	38	0.115	0.078	0.69
8.0	2.4	38	0.122	0.062	0.67
8.4	1.6	38	0.100	0.090	0.54
15.6	1.6	38	0.049	0.484	0.99

s:solid
p:porous

6. Conclusions and Recommendations

The major objective of this work was to determine an empirical correlation to estimate the maximum depth of penetration and the time to reach this depth for a high pressure water jet drilling into an oil sands formation. To this end a laboratory model was constructed to examine the characteristics of high pressure water jets jetting into a tube with one end closed. Flow visualization observations and records of the pressure at the bottom of the tube revealed that the water jet produced discrete impacts there. From this observation it was concluded that it is most appropriate to model the jet drilling as a stochastic process and to analyze the pressure signal statistically. By first requiring the probability of the pressure exceeding the critical value to be some non-zero value for non-negligible cutting rates to occur a correlation to predict the ultimate depth of penetration was developed. Secondly, by assuming a linear relation between drilling rate and the above probability, a second correlation predicting the depth of penetration with time was developed. These correlations are:

a. Maximum depth of penetration.

$$Z_{ult} = \sqrt{\{-\{d_o^2 \, P_d^k \, \ln c\}/a\}}$$

b. Depth at any instant in time.

$$t = \frac{1}{B} \int_0^z e^{\left\{\frac{a}{P_d^k}\right\}\left\{\frac{z}{d_o}\right\}^2} dz$$

Dynamic pressure range: 15 MPa to 35 MPa.

Nozzle diameter range: 1.6 mm to 3.2 mm.

Standoff distance range: 0.3 m to 1.7 m.

The results predicted from this correlation equation were found to agree fairly well with some limited field test data even though the assumed cutting model predicts the cutting rate to be independent of the pressure at the cutting face once the critical pressure is exceeded. A more complex cutting model was not pursued at this point for the laboratory data for establishing parameter values and field data for comparison purposes are both very limited.

Extrapolation of the model to field scale conditions predict ultimate depths of 6 meters for a dynamic pressure of 23 MPa in 6 minutes which are certainly of interest. In addition, water requirements can be made with these correlations and a 2.4 m^3 volume of water is predicted to reach that ultimate depth.

To further develop the stochastic approach utilized here to develop a cutting model, much more laboratory and field data of depth of penetration with time is required.

BIBLIOGRAPHY

Abramovich, G.N. *The Theory of Turbulent Jets*. The Massachusetts Institute of Technology Press, 1963.

Baughman, G.L. *Synthetic Fuels Data Handbook*. Second Edition, Cameron Engineers, Inc., Denver, Colorado, 1978.

Beckwith, T.G., and Buck, N.L. *Mechanical Measurements*. Second Edition, Addison-Wesley, 1973.

Bendat, J.S., and Piersol, A.G. *Random Data: Analysis and Measurement Procedures*. Wiley-Interscience, 1971.

Chau, W.T.R., "Jet Penetration of Oil Sands". M. Eng. Report, University of Alberta, Edmonton, 1980.

Crow, S.C., "A Theory of Hydraulic Rock Cutting," Int. J. Rock Mech. Min. Sci. & Geomech. Abstr., Vol. 10, pp. 567-584, 1973.

Davies, T.W., Metcalfe, R.A., and Jackson, M.K., "The Anatomy and Imapact Characteristics of Large Scale Water Jets", Fifth International Symposium on Jet Cutting Technology, June 1980.

Dusseault, M.B., "The Behaviour of Hydraulically Induced Fractures in Oil Sands", Canadian Rock Mech. Symp. Proc. 13th Underground Rock Engineering, Univ. of Toronto, Ontario, May 28-29, 1980, Publ. by CIM, Montreal, Quebec, pp. 36-41, 1980.

Erdmann-Jesnitzer, F., Louis, H., and Wiedemeier, J., "Rock Excavation with High Speed Water Jets", Fifth International Symposium on Jet Cutting Technology, June 1980.

Gates, E.M., and Toogood, R.W., "Modelling of Down-Hole Jet Piercing", AOSTRA report, to be published, 1983.

Gates, E.M., and Gilpin, R.R., "Jet Piercing of Oil Sands", Department of Mechanical Engineering, University of Alberta, Departmental Report No. 27, 1982.

Gerald, C.F., *Applied Numerical Analysis*. Second Edition, Addison Wesley, 1980.

Gilpin, R.R. and Gates E.M., "Jet Piercing of Oil Sands," Transactions of the ASME, Journal of Energy Resources Technology, Vol. 103, pp. 330-335, Dec. 1981.

Guttman, I., Wilks, S.S., and Hunter, J.S. *Introductory Engineering Statistics*. John Wiley & Sons, Inc., 1971.

Harnett, D.L., *Introduction to Statistical Methods*. Third Edition, Addison-Wesley, 1977.

Hashish, M. and duPlessis, M.P., "Theoretical and Experimental Investigation of Continuous Jet Penetration of Solids," Transactions of the ASME, Journal of Engineering for Industry, Vol. 100, No. 1, pp. 88-94, 1978.

Humphreys, R.D., and Schutte, R., "The Alberta Oil Sands: Energy for the Future", Proceedings of the Symposium on Oil Sand and Oil Shale Chemistry, Montreal, May 29 - June 2, 1977.

James, M.L., Smith, G.M., and Wolford, J.C. *Applied Numerical Methods for Digital Computation with Fortran and CSMP*. Second edition, Harper & Row, 1977.

Leach, S.J. and Walker, G.L., "Some Aspects of Rock Cutting by High Speed Water Jets," British Society of London, Philosophical Transactions, Series A, Vol. 260, pp. 295-308, 1966.

Lohn, P.D., and Brent, D.A., "Design and Test of an Inlet-Nozzle Device", Fourth International Symposium on Jet Cutting Technology, April 1978.

Puttagunta, V.R., Sochaski, R.O., and Robertson, R.F.S., "A Role for Nuclear Energy in the Recovery of Oil from the Tar Sands of Alberta", Journal of Canadian Petroleum Technology, Vol 16, Number 3, pp. 28-49, 1977.

Raisbeck, J.M., and Currie, J.B., "A Laboratory Investigation of Hydraulic Fracturing In Oil Sands", In Situ, Vol. 5, No. 1, pp. 1-24, 1981.

Singh, M.M., Labus, T.J., and Finlayson, L.A., "Field Testing of Water Jets for Coal Breakage", Second International Symposium on Jet Cutting Technology, April 1974.

Thomson, W.T. *Theory of Vibration With Applications*. Second Edition, Prentice Hall, 1981.

Wenk, E., Jr., "A Diaphragm-Type Gage for Measuring Low Pressures in Fluids", SESA Proc., Vol. 8, No. 2, pp. 90-96, 1951.

Werner, F.D., "The Design of Diaphragms for Pressure Gages Which Use the Bonded Wire Resistance Strain Gage", SESA

Proc., Vol. 11, No. 1, pp. 137-146, 1953.

Yahiro, T., Yoshida, H., and Nishi, K., "Sheet Piles Driving and H-Steel Pulling by High Speed Water Jets", Fifth International Symposium on Jet Cutting Technology, June 1980.

Yanaida, K. and Ohashi, A., "Flow Characteristics of Water Jets in Air", Fifth International Symposiun on Jet Cutting Technology, June 1980.

APPENDIX A

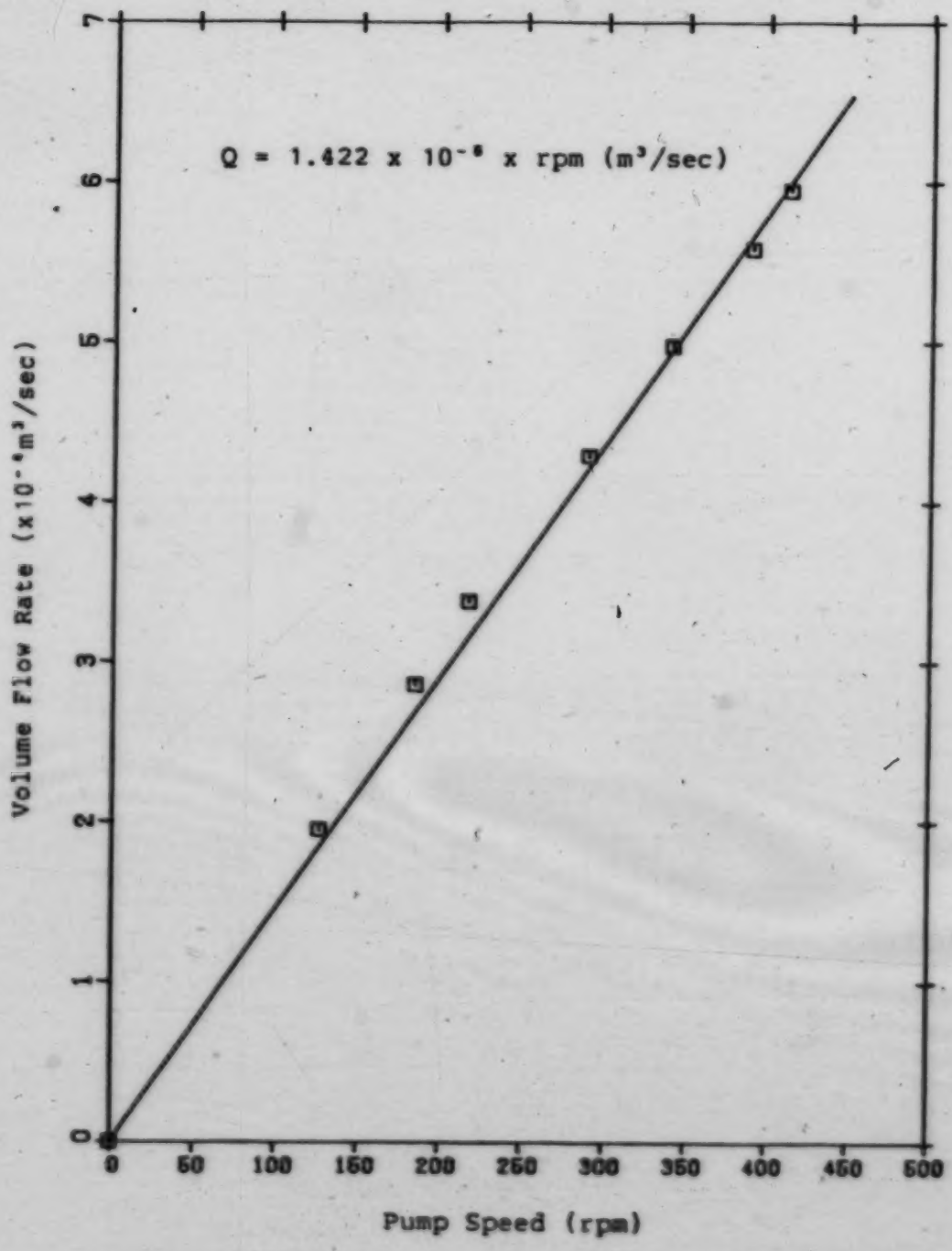

Figure A.1 Volume flow rate calibration curve.

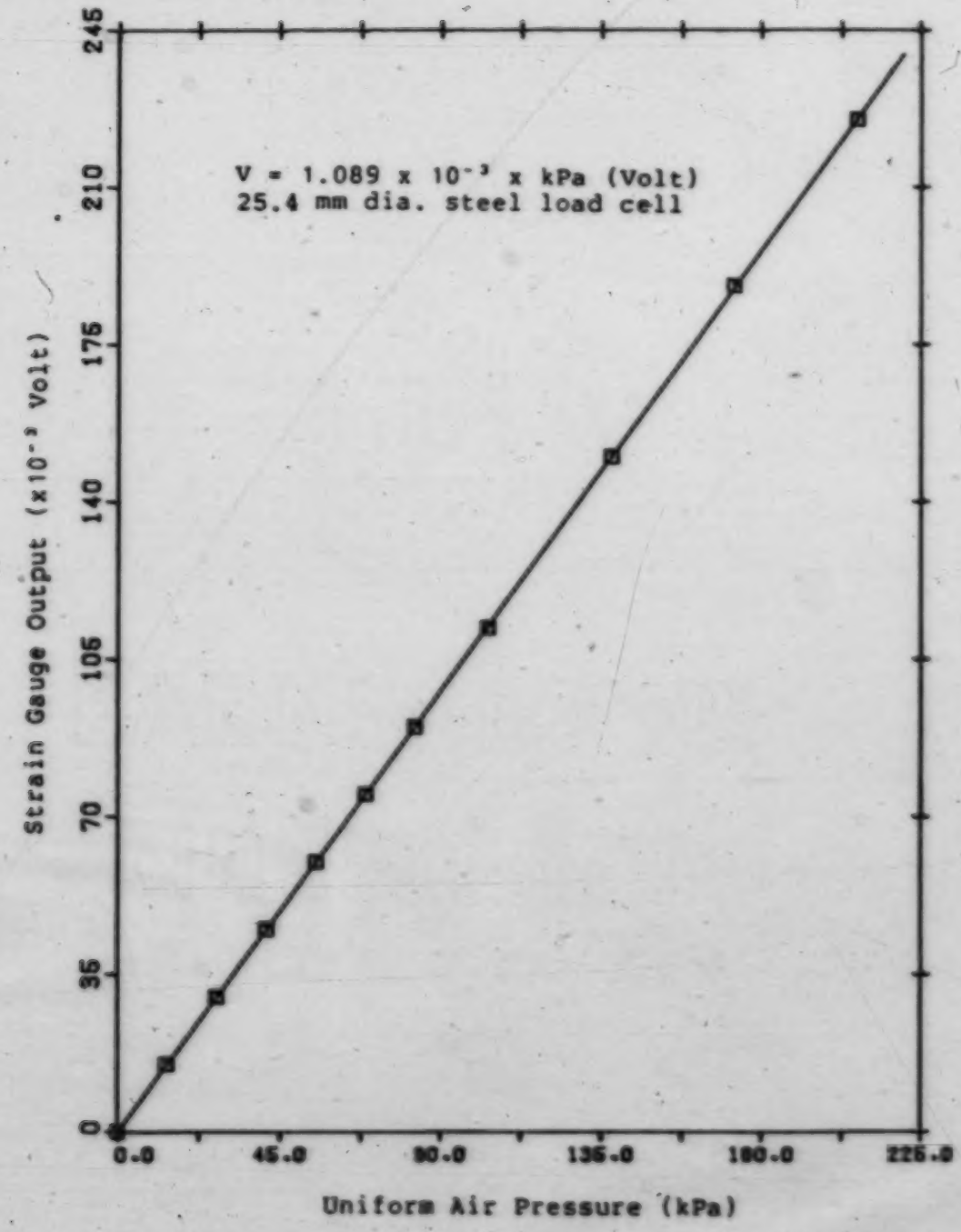

Figure A.2 Load cell calibration curve.

APPENDIX B

The value of the parameter B was determined using the limited laboratory data from Chau (1980). Chau obtained depths of penetration under different jetting times (up to 4 seconds) for various dynamic pressures. However, most of his data are limited to low dynamic pressures. From his observation, it was found that no cutting of oil sands occurs when the dynamic pressure falls below 1.2 MPa. Hence, to obtain a good estimate of the parameter B a higher dynamic pressure is essential. Therefore only the depths of penetration for higher dynamic pressure were used in determining the parameter B.

Using equation (9), that is:

$$B = \frac{1}{t}\int_0^z e^{\left\{\frac{a}{p_d^k}\right\}\left\{\frac{z}{d_o}\right\}^2} dz$$

and the measured depth of penetration by Chau, different values of B were obtained for different jetting times and pressures. As a result, for each dynamic pressure several values of B were obtained, as shown in figure B.1. This means that whenever 1 second jetting time was used, the corresponding depth of penetration calculated using equation (9) for 1 second jetting time coincides with the measured depth of penetration. The same thing is true for 2 seconds etc. However, the calculated depth of penetration for 2

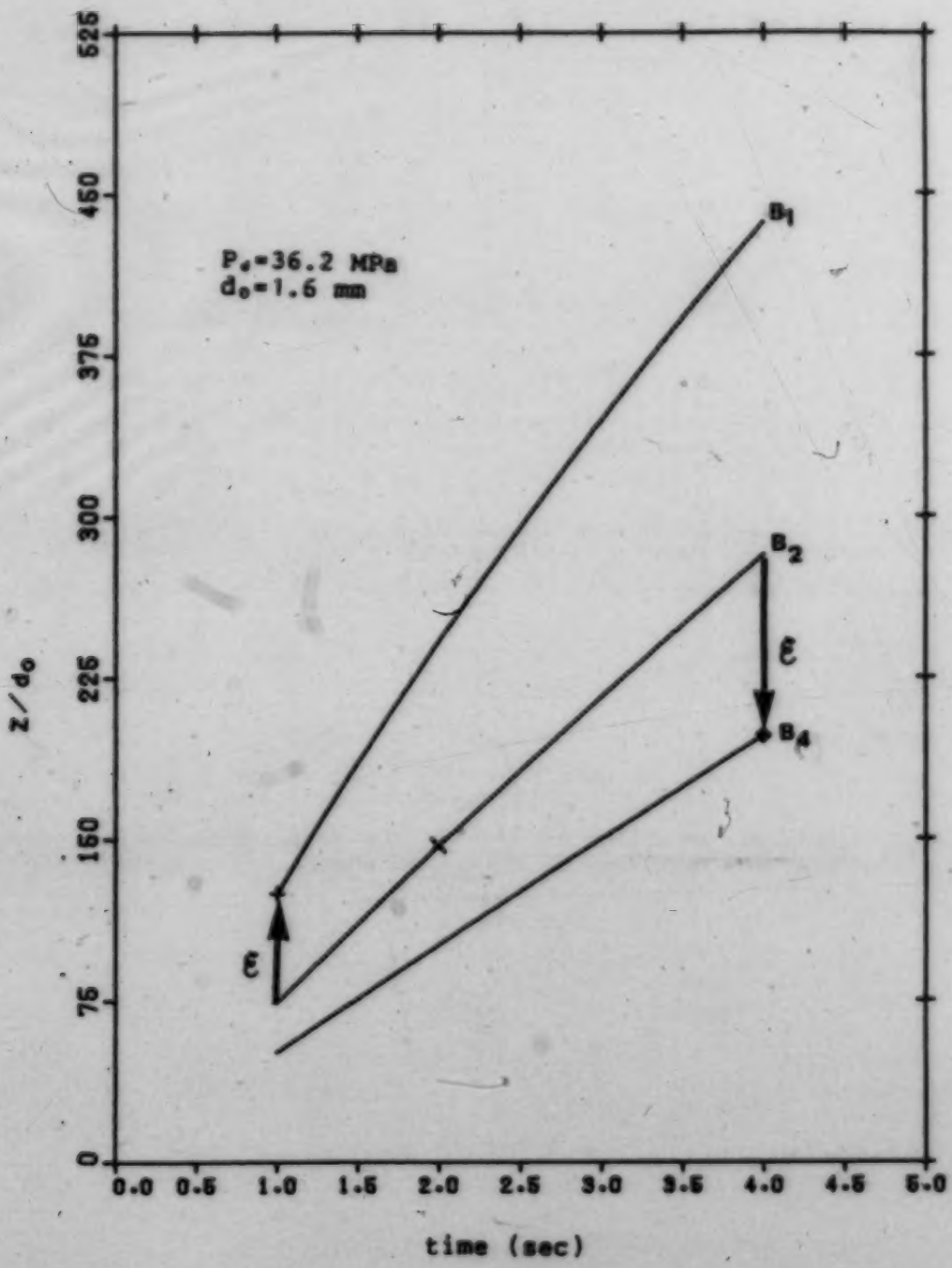

Figure B.1 A plot of the initial cutting rate using equation (9).

seconds using the value of B obtained for 1 second will not give the same result as the measured depth observed in 2 seconds shown in figure B.1. Therefore, the best values of B that will give the least error between the calculated depth of penetration and the measured values were determined. This was done by plotting the sum of the squares of the error, E, between measured depth and calculated depth to the values of B obtained for different jetting times as shown in figure B.2. The value of B that will give the minimum of this error summation was then chosen (ie. B4).

It appears from the data shown in figure B.1, that this procedure results in a conservative (ie. low) estimate for the initial cutting rate. More extensive experimental data is required to improve this estimation.

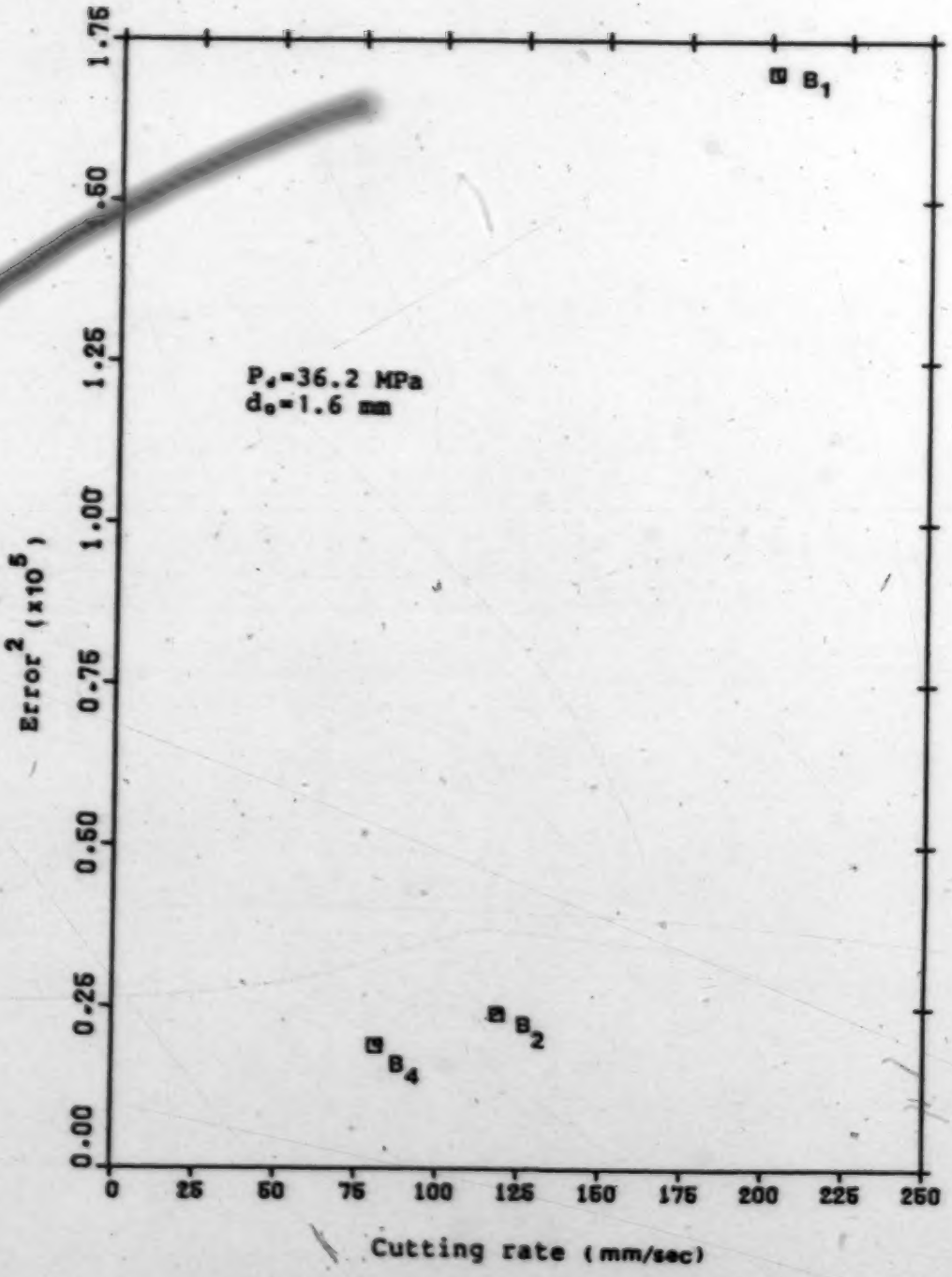

Figure B.2 Determination of the cutting rate.